Noname manuscript No.
(will be inserted by the editor)

Investigation of Painlevé's Paradox and Dynamic Jamming During Mechanism Sliding Motion

Yizhar Or · Elon Rimon

the date of receipt and acceptance should be inserted later

Abstract The paradox of Painlevé occurs when the dynamics of a sliding rigid body has solution inconsistency. When approaching a configuration of inconsistency, the contact forces and accelerations may grow unbounded in finite time, a scenario which is called *dynamic jamming*. Painlevé's paradox was originally formulated for a sliding rod with uniform mass distribution, for which inconsistency occurs only under unrealistically high contact friction conditions. This paper shows that when the sliding rod is replaced by a sliding mechanism, the dynamic jamming predicted by Painlevé's paradox can occur under relatively low friction. The paper proposes a particular mechanism, called IPOS, which consists of an inverted pendulum hinged to a plate that slides on an inclined plane. (IPOS = Inverted Pendulum On a Slider). The IPOS mechanism can reach solution inconsistency under practical friction conditions, and can thus be used to experimentally validate the theoretical predictions. The conditions under which dynamic jamming occurs in the IPOS mechanism dynamics are explicitly derived, and numerical simulations illustrate the feasibility of dynamic jamming experiments.

Keywords Nonsmooth mechanics · Painlevé's paradox · Multibody dynamics · Frictional contact

1 Introduction

The paradox of Painlevé occurs when the dynamics of a rigid body sliding under frictional contact has an inconsistent solution. When approaching a configuration of inconsistency, the contact forces and accelerations may grow unbounded in finite time, a scenario which is called *dynamic jamming*. At this instant the body experiences an abrupt impact event followed by immediate contact separation. Such singular events must be thoroughly understood and avoided in order to guarantee safe operation of legged robots [4,13,18,38], and agile robotic manipulation systems [8,20]. These systems are characterized by intermittent contacts, undergoing transitions from rolling to sliding to separation, and eventually back to contact via impact. When the interacting bodies are considered as ideally rigid, the contacts are modeled as unilateral constraints satisfying Coulomb's friction law [30,33,35]. The dynamic behavior of such systems is essentially non-smooth [2,5,16], and they are commonly modeled as hybrid dynamical systems [11], or as complementarity systems [1,29]. Such system may display unique phenomena such as finite-time Zeno sequence accumulation during contact establishment [26,40], and solution inconsistency during sliding [6,19,21] which stems from Painlevé's paradox.

Painlevé's classical paradox was introduced in 1895 [27], through a simple example of a uniform rod sliding with friction on a horizontal plane (Figure 1(a))[1]. Under a rigid body assumption and Coulomb's friction law, the rod's dynamics can reach events where its instantaneous solution is inconsistent with the model assumptions. Attempts to resolve this peculiarity involve two different theoretical approaches. One approach proposes the use of compliance models to describe the local contact deformation i.e., relaxation of the rigid body assumption [14,25,28,32]. A second approach proposes the incorporation of so-

Y. Or and E. Rimon are with the Faculty of Mechanical Engineering, Technion - Israel Institute of Technology, Haifa 32000, Israel. E-mail: {izi,rimon}@tx.technion.ac.il

[1] More accurately, the original study of Painlevé in [27] considered a rectangular block sliding on an inclined plane, see [15].

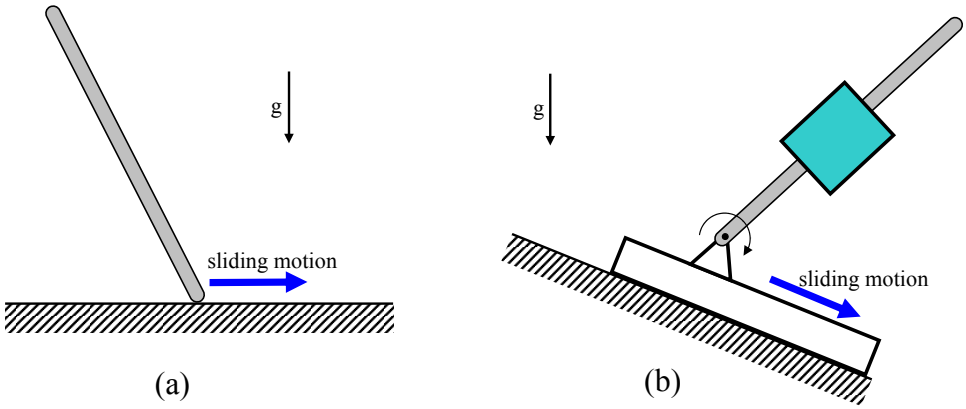

Fig. 1 (a) Sketch of Painlevé's sliding rod, and (b) the sliding IPOS mechanism.

lutions with impulsive (or measure-valued) contact forces into the rigid body paradigm, leading to development of time-stepping simulation schemes [23, 34]. The latter approach models contact jamming as tangential impact [37] or impact without collision [2], followed by immediate contact separation. Several papers study models of mechanical systems which display Painlevé's paradox. Examples are a rotating shaft [39], a robotic mechanism in contact with a conveyor belt [15,17], and a chalk sliding on a board [12]. However, the experimental demonstration of Painlevé's paradox is notoriously hard to achieve, mainly due to the fact that in Painlevé's original sliding rod example the paradox occurs only for an unrealistic friction coefficient of $\mu \geq 4/3$ [10]. Zhao et al. [41] describe an experiment where the tip of a double-pendulum mechanism is put in contact with a moving bar and displays periodic bouncing behavior of tangential impacts followed by contact separation. However, the occurence of dynamic jamming during rigid body sliding has not been validated in any experimental setting.

Following Dupont's terminology [7], *dynamic jamming* is the scenario where a rigid body subject to a frictional contact constraint starts in a consistent sliding motion under the influence of gravity or some other force, then reaches solution inconsistency in finite time. At this instant the contact reaction force appears to grow unbounded while the sliding contact reaches a sudden halt. Génot and Brogliato analyze the possibility of dynamic jamming in Painlevé's sliding rod example [10], though they use different terminology for this event. While Painlevé's paradox is feasible for $\mu \geq 4/3$, they have shown that when $4/3 \leq \mu < 8/3\sqrt{3}$ contact separation always precedes dynamic jamming. They have also shown that only when $\mu \geq 8/3\sqrt{3}$ there exist a range of initial sliding velocities that lead to dynamic jamming in finite time (although they do not specify how to compute these initial sliding velocities). Dynamic jamming can thus occur during rigid body sliding, but requires an unrealistically high friction coefficient of $\mu \geq 1.54$ (where $8/3\sqrt{3} \cong 1.54$).

The main contribution of this paper is extension of the analysis in [10] which studied Painlevé's example of a rod sliding under point contact to a mechanism sliding under line contact. We establish that for this sliding mechanism, dynamic jamming is feasible under significantly lower friction conditions. The paper proposes a specific mechanism that mimics Painlevé's classical sliding rod example. The mechanism, called IPOS for Inverted Pendulum on a Slider, consists of a heavy rod hinged to a light plate which slides on an inclined plane (Figure 1(b)). The rod has a *non-uniform* mass distribution achieved by a heavy mass at its center. Generalizing the analysis of Génot and Brogliato in [10], the paper then derives an expression for the minimal friction coefficient above which IPOS may experience solution inconsistency (analogous to $\mu = 4/3$ in [10]). Then it determines the critical friction coefficient above which suitable initial sliding velocities lead to dynamic jamming (analogous to $\mu = 8/3\sqrt{3}$ in [10]). The paper also derives explicit conditions on the initial configuration and velocity of the IPOS that lead to dynamic jamming. Finally, the paper selects specific parameter values and illustrates with simulations how the IPOS mechanism can experimentally verify the dynamic jamming predictions.

The paper is organized as follows. The next section formulates the dynamics of a generic mechanism sliding on an inclined plane and shows how dynamic jamming can occur during this motion. Section 3 describes the IPOS mechanism and provides an expression for its specific dynamic equation. Sections 4 and 5 contain a theoretical analysis of Painlevé's paradox and dynamic jamming in the IPOS mechanism. Section 6 demonstrates with simulations how proper parameter values can induce dynamic jamming under practical friction conditions. The concluding sec-

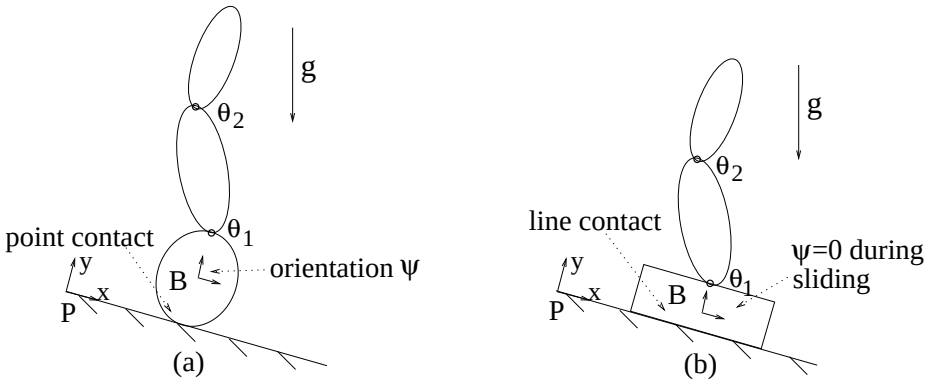

Fig. 2 A mechanism sliding on an inclined plane with (a) point, and (b) line contact.

tion discusses preliminary experiments and future research directions.

2 Occurrence of Dynamic Jamming During Mechanism Sliding Motion

This section formulates the dynamics of a planar sliding mechanism and describes how dynamic jamming can arise during this motion. The mechanism's dynamics is first described for a mechanism sliding with *point contact*, then for a mechanism sliding with *line contact*. The latter case corresponds to the IPOS mechanism introduced in the next section. The formulation follows the standard scheme of Euler-Lagrange equations under configuration constraints, cf. [30].

2.1 Formulation of Mechanism Sliding Dynamics

Let $\mathcal{K}$ be a planar mechanism of rigid bodies connected by passive rotational joints. One body of the mechanism, $\mathcal{B}$, slides with *point contact* on an inclined plane P (Figure 2(a)). We assume Coulomb friction at the contact, and assume that gravity or some other force maintains the sliding motion during a time interval. The mechanism's dynamics takes place in its constrained configuration space. Let (x, y, ψ) denote the position and orientation of the sliding body $\mathcal{B}$ with respect to a fixed reference frame. Let $(\theta_1, \ldots, \theta_n)$ denote the mechanism's joints. The configuration of $\mathcal{K}$ is parametrized by $q = (x, y, \theta_1, \ldots \theta_n, \psi) \in \mathbb{R}^{n+3}$, where the choice of ψ as the last coordinate is merely a notational convenience. The plane P imposes the following constraint on the configurations of $\mathcal{K}$. Let $\mathcal{B}(q)$ be the set in $\mathbb{R}^2$ occupied by the body $\mathcal{B}$ when the mechanism is at a configuration q. Let $d(q)$ be the minimal Euclidean distance between $\mathcal{B}(q)$ and P ($d(q)$ is a smooth function when $\mathcal{B}$ is locally smooth at the contact). Then $d(q) = 0$ during any contact preserving motion of $\mathcal{K}$, while $d(q) > 0$ during any contact breaking motion of $\mathcal{K}$.

Next we introduce notation for the contact point velocity components. Let $\boldsymbol{x}(q)$ denote the contact point position in the fixed reference frame. Let $\hat{t}$ and $\hat{n}$ be the unit tangent and unit normal to P, such that $\hat{n}$ points outward with respect to P. The tangential and normal components of the contact point velocity, $\dot{\boldsymbol{x}}(q)$, are given by $v_t = \hat{t} \cdot \dot{\boldsymbol{x}}(q)$ and $v_n = \hat{n} \cdot \dot{\boldsymbol{x}}(q)$. Let $D\boldsymbol{x}(q)$ be the Jacobian matrix of $\boldsymbol{x}(q)$. Then $v_t = \boldsymbol{w}_t(q) \cdot \dot{q}$ where $\boldsymbol{w}_t(q) = D\boldsymbol{x}(q)^T \hat{t}$, while $v_n = \boldsymbol{w}_n(q) \cdot \dot{q}$ where $\boldsymbol{w}_n(q) = D\boldsymbol{x}(q)^T \hat{n}$. Note that v_n can also be written as $v_n = \nabla d(q) \cdot \dot{q}$, so that $\boldsymbol{w}_n(q) = \nabla d(q)$.

Denote by f the reaction force acting on $\mathcal{B}$ at $\boldsymbol{x}(q)$, and by $f_t = \hat{t} \cdot f$ and $f_n = \hat{n} \cdot f$ the tangential and normal components of f. When the contact is sliding $v_t \neq 0$, Coulomb's friction law imposes the relation

$$f_t = -\sigma \mu f_n \qquad \sigma = \mathsf{sgn}(v_t), \tag{1}$$

where μ is the friction coefficient. Let $\boldsymbol{F}(q)$ denote the generalized force induced on the mechanism by f.[2] Based on the virtual work principle [31], $\boldsymbol{F}(q)$ is given by $\boldsymbol{F}(q) = D\boldsymbol{x}(q)^T f$. Since $f = f_n(\hat{n} - \sigma\mu\hat{t})$ during sliding, the generalized force can be written as $\boldsymbol{F}(q) = f_n\big(\boldsymbol{w}_n(q) - \sigma\mu\boldsymbol{w}_t(q)\big)$. The dynamic equation of the sliding mechanism is given by

$$M(q)\ddot{q} + H(q, \dot{q}) + G(q) = f_n \left(\boldsymbol{w}_n(q) - \sigma\mu\boldsymbol{w}_t(q)\right), \tag{2}$$

where $M(q)$ is the mechanism's inertia matrix, $H(q, \dot{q})$ is the vector of Coriolis and centripetal terms, and $G(q)$ is the generalized force induced by potential forces such as gravity, elastic elements, or else. Note that (2) captures the mechanism's dynamics during sliding as well as during contact separation. In the latter case substituting $f_n = 0$ in (2) gives the contact separation dynamics. Nevertheless, (2) in its present

[2] Formally, $\boldsymbol{F}(q)$ is a covector based at q, which acts on tangent vectors $\dot{q}$ via the Euclidean inner product $\boldsymbol{F} \cdot \dot{q}$.

case	sgn(A)	sgn(B)	solution	physical meaning
1	+	+	$a_n = 0,\ f_n = \frac{A}{B} > 0$	consistent sliding
2	-	+	$f_n = 0,\ a_n = -A > 0$	consistent separation
3	-	-	$f_n = 0,\ a_n = -A > 0$ **or** $a_n = 0,\ f_n = \frac{A}{B} > 0$	indeterminacy
4	+	-	$\emptyset$	inconsistency

Table 1 Summary of the possible contact interactions during sliding motion.

form does *not* capture the case of *rolling contact* (i.e. tangential sticking), in which the tangential velocity v_t vanishes and the contact force satisfies $|f_t| \leq \mu f_n$. That is, the sign function in (1) is not defined at $v_t = 0$ (more precisely, it is set-valued with the interval $[-1, 1]$).

Painlevé's paradox is based on the expression for the contact point normal acceleration, $a_n = \dot{v}_n$, along solutions of (2). Since $v_n = \boldsymbol{w}_n(q) \cdot \dot{q}$, the contact point normal acceleration is given by $a_n = \boldsymbol{w}_n(q) \cdot \ddot{q} + \dot{q}^T D\boldsymbol{w}_n(q)\dot{q}$. Substituting the solution for $\ddot{q}$ from (2) in the expression for a_n gives

$$a_n = \boldsymbol{w}_n^T(q)M^{-1}(q)\big(-H(q,\dot{q}) - G(q) + f_n(\boldsymbol{w}_n(q) - \sigma\mu\boldsymbol{w}_t(q))\big) + \dot{q}^T D\boldsymbol{w}_n(q)\dot{q}. \tag{3}$$

Collecting the terms of (3) in a compact form gives the key expression ([10]):

$$a_n = -A(q,\dot{q}) + B(q,\mu)f_n \tag{4}$$

where

$$A(q,\dot{q}) = \boldsymbol{w}_n^T(q)M^{-1}(q)\left(H(q,\dot{q}) + G(q)\right) - \dot{q}^T D\boldsymbol{w}_n(q)\dot{q}$$
$$B(q,\mu) = \boldsymbol{w}_n^T(q)M^{-1}(q)\left(\boldsymbol{w}_n(q) - \mu\sigma\boldsymbol{w}_t(q)\right). \tag{5}$$

Note that B depends on $\dot{q}$ via the sign variable $\sigma = \mathsf{sgn}(v_t)$. However, the sliding direction and hence σ is constant during any particular sliding interval.

Consider the situation where the mechanism slides with positive tangential velocity during a time interval $t \in (-\epsilon, 0)$. During this time interval $a_n = 0$ while $f_n > 0$. If the tangential velocity is non-vanishing at $t = 0$, the instantaneous solution of (4) at this instant can be either continuation of sliding or contact separation. That is, a_n and f_n in (4) must satisfy the linear complementarity relation $0 \leq a_n \perp f_n \geq 0$ (cf. [1,29]). In the case of sliding (4) becomes $0 = -A + Bf_n$. Since $f_n > 0$ during sliding, this dictates that $\mathsf{sgn}(A) = \mathsf{sgn}(B)$ at $t = 0$. In the case of contact separation $f_n = 0$ while $a_n > 0$. In this case (4) becomes $a_n = -A$. Since $a_n > 0$ during contact separation, this dictates that $A < 0$ at $t = 0$. The contact interactions can thus be classified according to the sign of A and B at $t = 0$. The four possible cases are summarized in Table 1. Case 1 where $A > 0$ and $B > 0$ corresponds to *consistent sliding.* Case 2 where $A < 0$ and $B > 0$ corresponds to *consistent separation.* Case 3 where $A < 0$ and $B < 0$ is *indeterminate*, as it corresponds to either sliding or separation[3]. Case 4 where $A > 0$ and $B < 0$ cannot correspond to sliding since (4) gives $f_n < 0$, nor to contact separation since (4) gives $a_n < 0$. This case is therefore physically infeasible. Following the terminology in Génot and Brogliato [10], the $(q, \dot{q})$ region delineated by $A(q, \dot{q}) > 0$ and $B(q, \mu) < 0$ is the *inconsistency region.* When a solution approaches the boundary of this region it exhibits a peculiar behavior called dynamic jamming, which is defined as follows.

Definition 1 ***Dynamic jamming*** *is the scenario where a mechanism $\mathcal{K}$ starts with a consistent and determinate sliding motion and approaches the solution inconsistency region with $B(q, \mu) \to 0$.*

Note that the definition focuses only on solutions from case 1 in Table 1, where sliding is the only consistent solution. Since $f_n = A(q, \dot{q})/B(q, \mu)$ during a consistent sliding motion, the reaction force magnitude appears to grow unbounded when $B(q, \mu)$ approaches zero. The detailed behavior of the solution during this event is analyzed in Section 4.

2.2 Mechanism Sliding Dynamics with Line Contact

The IPOS mechanism introduced in the next section maintains line contact during sliding. Let us therefore extend the mechanism's dynamics to the case where its sliding body, $\mathcal{B}$, is a rectangular body that maintains *line contact* with the inclined plane P. Let a fixed reference frame be located at the top of P, with its x-axis pointing downward along P and its y-axis pointing upward with respect to P (Figure 2(b)). During sliding with line contact $\mathcal{B}$'s orientation, ψ, remains constant with respect to the fixed reference frame.

The contact reaction force acting on $\mathcal{B}$ is now distributed along a contact segment. To capture the force distribution in a compact form, fix a body frame to $\mathcal{B}$ at a point $b \in \mathcal{B}$. Let I denote the contact

[3] Note that resolution of this indeterminacy is proposed in [25] by using the limit of a compliant contact model.

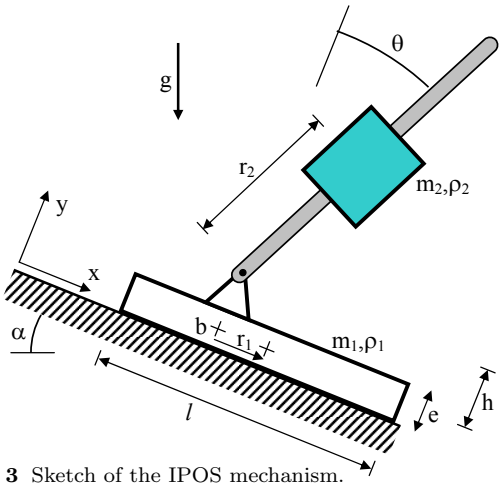

Fig. 3 Sketch of the IPOS mechanism.

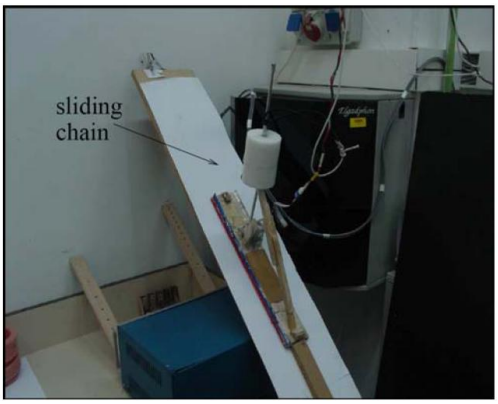

Fig. 4 A prototype of the IPOS mechanism sliding on an inclined plane under the influence of gravity.

segment, and let $f(x) = (f_t(x), f_n(x))$ for $x \in I$ be the local contact force distribution. The net tangential and normal components of the force distribution, $f_t = \int_{x\in I} f_t(x)dx$ and $f_n = \int_{x\in I} f_n(x)dx$, still satisfy the relation $f_t = -\sigma\mu f_n$ during sliding. Let $\tau \in \mathbb{R}$ be the net moment generated about $\mathcal{B}$'s origin by the normal component of the force distribution, $f_n(x)$ for $x \in I$, that is, $\tau = \int_{x\in I}(x-b)\times \hat{n} f_n(x)dx$. The dynamic equation governing the mechanism's sliding motion with line contact is given by

$$M(q)\ddot{q}+H(q,\dot{q})+G(q) = f_n\big(\boldsymbol{w}_n(q)-\sigma\mu\boldsymbol{w}_t(q)\big)+\tau\boldsymbol{w}_\psi, \tag{6}$$

where $\boldsymbol{w}_\psi = (0,\ldots,0,1)$.

We now derive an expression of the form $a_n = -A + Bf_n$ along solutions of (6). First consider the moment τ generated by the normal force distribution. Since $\psi = 0$ during sliding with line contact, $\ddot{\psi} = 0$ along this motion. The latter condition can be written as $\boldsymbol{w}_\psi \cdot \ddot{q} = 0$ (since ψ is the last coordinate of q). Substituting the solution for $\ddot{q}$ from (6) in $\boldsymbol{w}_\psi \cdot \ddot{q} = 0$ and solving for τ gives

$$\begin{aligned}\tau(q,\dot{q},f_n) = \tfrac{1}{\boldsymbol{w}_\psi^T M^{-1}(q)\boldsymbol{w}_\psi}\boldsymbol{w}_\psi^T M^{-1}(q)\big(H(q,\dot{q})+G(q)\\ -f_n\left(\boldsymbol{w}_n(q)-\sigma\mu\boldsymbol{w}_t(q)\right)\big).\end{aligned} \tag{7}$$

Let v_n and a_n be the normal velocity and normal acceleration of $\mathcal{B}$'s origin. Then $v_n = \boldsymbol{w}_n(q)\cdot q$, and consequently $a_n = \boldsymbol{w}_n(q)\cdot\ddot{q} + \dot{q}^T D\boldsymbol{w}_n(q)\dot{q}$. Substituting the solution for $\ddot{q}$ from (6) in this expression gives

$$\begin{aligned}a_n = \boldsymbol{w}_n^T(q)M^{-1}(q)\left(-H(q,\dot{q})-G(q)+f_n(\boldsymbol{w}_n(q)-\sigma\mu\boldsymbol{w}_t(q))\right.\\ \left.+\boldsymbol{w}_\psi(q)\tau\right)+\dot{q}^T D\boldsymbol{w}_n(q)\dot{q}\end{aligned}.$$

Substituting for τ according to (7) and collecting terms, we obtain a governing equation similar to (4):

$$a_n = -A(q,\dot{q}) + B(q,\mu)f_n \tag{8}$$

where

$$\begin{aligned}A(q,\dot{q}) &= \boldsymbol{w}_n^T(q)M^{-1}(q)W(q)\left(H(q,\dot{q})+G(q)\right)-\dot{q}^T D\boldsymbol{w}_n(q)\dot{q}\\ B(q,\mu) &= \boldsymbol{w}_n^T(q)M^{-1}(q)W(q)\left(\boldsymbol{w}_n(q)-\mu\sigma\boldsymbol{w}_t(q)\right)\\ W(q) &= \mathbf{I} - \frac{1}{\boldsymbol{w}_\psi^T M^{-1}(q)\boldsymbol{w}_\psi}\boldsymbol{w}_\psi\boldsymbol{w}_\psi^T M^{-1}(q),\end{aligned} \tag{9}$$

and $\mathbf{I}$ is the identity matrix. The possible contact interactions during sliding are still captured by the four cases of Table 1. In particular, *dynamic jamming* is defined in the same manner as above: the mechanism starts with consistent sliding motion and approaches solution inconsistency with $B(q(t),\mu) \to 0$.

3 The IPOS Mechanism

This section describes the IPOS mechanism and its dynamic equations. The mechanism consists of two bodies hinged by a passive revolute joint, as sketched in Figure 3. The lower body is a rectangular block which maintains line contact with an inclined plane. The upper body is a pivoting rod which resembles Painlevé's rod. The IPOS mechanism thus forms an inverted pendulum, which slides on a line contact under the influence of gravity. A preliminary experimental prototype of the IPOS mechanism is shown in Figure 4. It consists of a heavy vertical rod hinged to a flat slider which is much lighter than the rod. The diagonal beam at the slider's front locks the hinge until the mechanism reaches the desired initial sliding velocity. At this instant the beam is broken by a string attached to the back wall, and the mechanism starts its downward sliding motion with a freely rotating hinge. Preliminary motion experiments with this mechanism [22] showed that it currently does not operate under sufficiently large friction in order

to display dynamic jamming, as discussed further in the concluding section.

The IPOS mechanism is described by the following parameters. The lower body, the *slider,* has length l, thickness e, and mass m_1. The upper body, the *rod,* has half-length r_2 and mass m_2. The hinge connecting the rod to the slider is located at a height $h+e/2$ above the inclined plane. While the slider has a uniform mass distribution, the rod has a *non-uniform* mass distribution due to a heavy mass at its center. The bodies' mass distribution is described by their radius of gyration.[4] The slider has a radius of gyration ρ_1, the rod has a radius of gyration ρ_2. Finally, the inclined plane P has a slope angle α. A list of the IPOS parameters is summarized in Table 2.

Symbol	Description
l	slider length
e	slider thickness
r_2	rod half-length
m_1	slider mass
m_2	rod mass
ρ_1	slider radius of gyration
ρ_2	rod radius of gyration
$\mathbf{b}$	slider frame origin
h	height of hinge above $\mathbf{b}$
r_1	distance between $\mathbf{b}$ and slider center
α	slope angle of inclined plane

Table 2 List of IPOS parameters.

Let a fixed reference frame be located at the top of the inclined plane P as shown in Figure 3. Let a body frame be fixed to the slider at a point $\mathbf{b}$, such that $\mathbf{b}$ is located at a height of $e/2$ above P and at a distance r_1 behind the slider's center. The configuration of IPOS is parametrized by $q=(x,y,\theta,\psi)\in I\!R^4$, where (x,y,ψ) is the position and orientation of the slider, and $\theta\in[-\pi/2,\pi/2]$ is the hinge angle. The hinge angle θ is measured in clockwise direction with respect to the y-axis of the fixed reference frame. The dynamic equation of the IPOS mechanism takes the form (6),

$$\begin{aligned} &M(q)\ddot{q}+H(q,\dot{q})+G(q)= \\ &\quad f_n\left(\boldsymbol{w}_n(q)-\sigma\mu\boldsymbol{w}_t(q)\right)+\tau(q,\dot{q},f_n)\boldsymbol{w}_\psi, \end{aligned} \tag{10}$$

where $\boldsymbol{w}_n=(0,1,0,0)$, $\boldsymbol{w}_t=(1,0,0,e/2)$, $\boldsymbol{w}_\psi=(0,0,0,1)$. The expressions for $M(q)$, $H(q,\dot{q})$, and $G(q)$ are given in Table 3, where S and C denote sine and cosine functions, and g is the gravitational constant. During sliding with line contact, since $\psi=\dot{\psi}=0$ the expressions for M, H, and G are simpler and depend only on θ and $\dot{\theta}$:

$$M(\theta)=\begin{bmatrix} m_1+m_2 & 0 & m_2r_2C\theta & m_2h \\ 0 & m_1+m_2 & -m_2r_2S\theta & -m_1r_1 \\ m_2r_2C\theta & -m_2r_2S\theta & m_2(r_2^2+\rho_2^2) & m_2hr_2C\theta \\ m_2h & -m_1r_1 & m_2hr_2C\theta & m_1(r_1^2+\rho_1^2)+m_2h^2 \end{bmatrix}$$

$$H(\theta,\dot{\theta})=\begin{pmatrix} -m_2r_2\dot{\theta}^2S\theta \\ -m_2r_2\dot{\theta}^2C\theta \\ 0 \\ -m_2r_2h\dot{\theta}^2S\theta \end{pmatrix} \quad G(\theta)=\begin{pmatrix} -(m_1+m_2)gS\alpha \\ (m_1+m_2)gC\alpha \\ -m_2r_2g\sin(\theta+\alpha) \\ -m_1r_1gC\alpha-m_2ghS\alpha \end{pmatrix}. \tag{11}$$

The expressions for A and B in the governing equation, $a_n=-A+Bf_n$, are obtained by substituting (11) into (9). Noting that $D\boldsymbol{w}_n(q)=0$ in (9), A and B depend only on $(\theta,\dot{\theta})$ and are given by

$$A(\theta,\dot{\theta})=g\cos\alpha-r_{eq}\dot{\theta}^2\cos\theta$$

$$B(\theta,\mu)=$$

$$\frac{1}{m_{eq}}\left(\left(1+\frac{m_1}{m_2}\right)\left(1+\frac{\rho_2^2}{r_2^2}\right)-\cos^2\theta+\sigma\mu\sin\theta\cos\theta\right)$$

$$\text{where}\quad m_{eq}=\frac{(m_1+m_2)(m_1(r_2^2+\rho_2^2)+m_2\rho_2^2)}{m_2r_2^2}$$

$$\text{and}\quad r_{eq}=\frac{m_2}{m_1+m_2}r_2. \tag{12}$$

The equation $a_n=-A+Bf_n$ is thus completely specified within the $(\theta,\dot{\theta})$ plane. When the rod has a uniform mass distribution, its radius of gyration is $\rho_2^2=r_2^2/3$. When such a rod slides on a horizontal plane without a slider ($\alpha=0$ and $m_1=0$), the expressions in (12) reduce with minor notational differences to those obtained for Painlevé's original example in [10].

Finally consider the condition under which the slider maintains its line contact with the inclined plane P. The condition is obtained by lumping the normal force distribution acting on the slider into a single force of magnitude f_n acting at a point $\boldsymbol{x}\in P$. Consider the net torque τ exerted by the normal force distribution about $\mathbf{b}$, measured in clockwise direction. The location of $\boldsymbol{x}$ is determined by the requirement that the lumped normal force generates the torque τ, $f_n(\boldsymbol{x}-b)\cdot\hat{t}=\tau$. The slider maintains its line contact with P as long as $\boldsymbol{x}$ lies within the contact segment I. The contact segment is delineated by $l/2\le(\boldsymbol{x}-b)\cdot\hat{t}+r_1\le l/2$, where l is the slider's length and r_1 is the distance between $\mathbf{b}$ and the slider's center. The line contact condition is

[4] The radius of gyration of a planar body is $\rho=\sqrt{J/m}$, where m is the body's mass and J is the body's moment of inertia about its center of mass. It has length units and satisfies the relation $J=m\rho^2$.

$$\mathrm{M(q)}=\begin{bmatrix} m_1{+}m_2 & 0 & m_2r_2C\theta & -m_1r_1S\psi + m_2hC\psi \\ 0 & m_1{+}m_2 & -m_2r_2S\theta & -m_1r_1C\psi - m_2hS\psi \\ m_2r_2C\theta & -m_2r_2S\theta & m_2(r_2^2{+}\rho_2^2) & m_2hr_2\cos(\theta-\psi) \\ -m_1r_1S\psi + m_2hC\psi & -m_1r_1C\psi - m_2hS\psi & m_2hr_2\cos(\theta-\psi) & m_1(r_1^2{+}\rho_1^2){+}m_2h^2 \end{bmatrix}$$

$$H(q,\dot{q})=\begin{pmatrix} -(m_1r_1C\psi + m_2hS\psi)\dot{\psi}^2 - m_2r_2\dot{\theta}^2S\theta \\ (m_1r_1S\psi - m_2hC\psi)\dot{\psi}^2 - m_2r_2\dot{\theta}^2C\theta \\ m_2r_2h\dot{\psi}^2\sin(\theta-\psi) \\ -m_2r_2h\dot{\theta}^2\sin(\theta-\psi) \end{pmatrix}, \quad G(q)=\begin{pmatrix} -(m_1{+}m_2)gS\alpha \\ (m_1{+}m_2)gC\alpha \\ -m_2r_2g\sin(\theta+\alpha) \\ -m_1r_1g\cos(\psi+\alpha) - m_2gh\sin(\psi+\alpha) \end{pmatrix},$$

Table 3 Expressions for $M(q)$, $H(q,\dot{q})$ and $G(q)$ of the IPOS mechanism.

thus specified by

$$-\frac{l}{2} \le \frac{\tau}{f_n} + r_1 \le \frac{l}{2}. \tag{13}$$

The formula for τ in these inequalities is based on (7) and is given by

$$\tau(\theta,\dot{\theta}) = C_\tau(\theta,\mu)\frac{A(\theta,\dot{\theta})}{B(\theta,\mu)} + D_\tau(\theta,\dot{\theta}), \tag{14}$$

where A and B are specified in (12) while C_τ and D_τ are given by

$$\begin{aligned} C_\tau(\theta,\mu) &= -\frac{1}{\boldsymbol{w}_\psi^T M^{-1}(q)\boldsymbol{w}_\psi}\boldsymbol{w}_\psi^T M^{-1}(q)(\boldsymbol{w}_n(q) - \sigma\mu\boldsymbol{w}_t(q)) \\ D_\tau(\theta,\dot{\theta}) &= \frac{1}{\boldsymbol{w}_\psi^T M^{-1}(q)\boldsymbol{w}_\psi}\boldsymbol{w}_\psi^T M^{-1}(q)(H(q,\dot{q}) + G(q)). \end{aligned} \tag{15}$$

(Note that C_τ and D_τ depend only on $(\theta,\dot{\theta})$, since M, H, and G depend only on $(\theta,\dot{\theta})$.) Condition (13) guarantees that the contact force distribution can generate the net torque required to satisfy the constraint $\psi = 0$ (and hence the line contact). When $\boldsymbol{x}$ emerges outside the contact segment the slider can no longer maintain its line contact with P. The ensuing *tipover motion* where the slider continues sliding on its tip is further considered in Section 5.

4 Dynamic Jamming in the IPOS Mechanism

This section characterizes the conditions for occurrence of dynamic jamming in the IPOS mechanism, by generalizing Génot and Brogliato's analysis [10]. We first determine the boundary of the inconsistency region in the $(\theta,\dot{\theta})$ plane, then determine which solution trajectories can reach this boundary. Some IPOS trajectories do reach a particular corner point of the inconsistency region, and a detailed analysis of the trajectories in the vicinity of this point follows.

4.1 IPOS Dynamic Jamming Condition

The IPOS mechanism reaches dynamic jamming when a consistent sliding trajectory approaches the inconsistency region with $B(\theta(t),\mu) \to 0$. As specified in Table 1, $B(\theta,\mu) > 0$ during consistent sliding while $B(\theta,\mu) < 0$ in the inconsistency region. Hence we first study the conditions for negativity of B. Let $\gamma = \arctan(\mu)$ be the friction cone half-angle. Using eq. (12), the expression for $B(\theta,\mu)$ in the case of forward sliding ($\sigma = +1$) can be written as

$$B(\theta,\mu) = \frac{1}{2m_{eq}}\left(\kappa - \sqrt{1+\mu^2}\cos(2\theta+\gamma)\right), \tag{16}$$

where m_{eq} is specified in (12) and κ is given by

$$\kappa = 2\left(1{+}\frac{m_1}{m_2}\right)\left(1{+}\frac{\rho_2^2}{r_2^2}\right) - 1. \tag{17}$$

The parameter κ depends on two key components of the mechanism's overall mass distribution: the rod and slider mass ratio, m_1/m_2, and the rod's gyration ratio, ρ_2/r_2.

The equation $B(\theta,\mu) = 0$ delineates the boundary of the inconsistency region in the $(\theta,\dot{\theta})$ plane. The equation can have zero or two solutions in the interval $\theta \in [-\pi/2, \pi/2]$. It has two solutions if and only if $\kappa < \sqrt{1+\mu^2}$, and in this case the two solutions delineate an interval where $B(\theta,\mu) < 0$. For any fixed κ, an interval where $B(\theta,\mu) < 0$ exists only when the friction coefficient is *sufficiently large,* $\mu > \mu_{min}$ where $\mu_{min} = \sqrt{\kappa^2 - 1}$. The way to decrease μ_{min} and thus enlarge the range of the mechanism's inconsistent configurations is by setting the ratios m_1/m_2 and ρ_2/r_2 as small as possible. That is, the slider should be much lighter than the rod, while the rod should have most of its mass concentrated close to its center. For any $\mu > \mu_{min}$, inconsistency configurations where $B(\theta,\mu) < 0$ are associated with $\theta \in [\theta_{c1}, \theta_{c2}]$, where the critical angles θ_{c1} and θ_{c2} are given by

$$\theta_{c1,c2} = -\frac{1}{2}\left(\gamma \mp \arccos\left(\frac{\kappa}{\sqrt{1+\mu^2}}\right)\right). \tag{18}$$

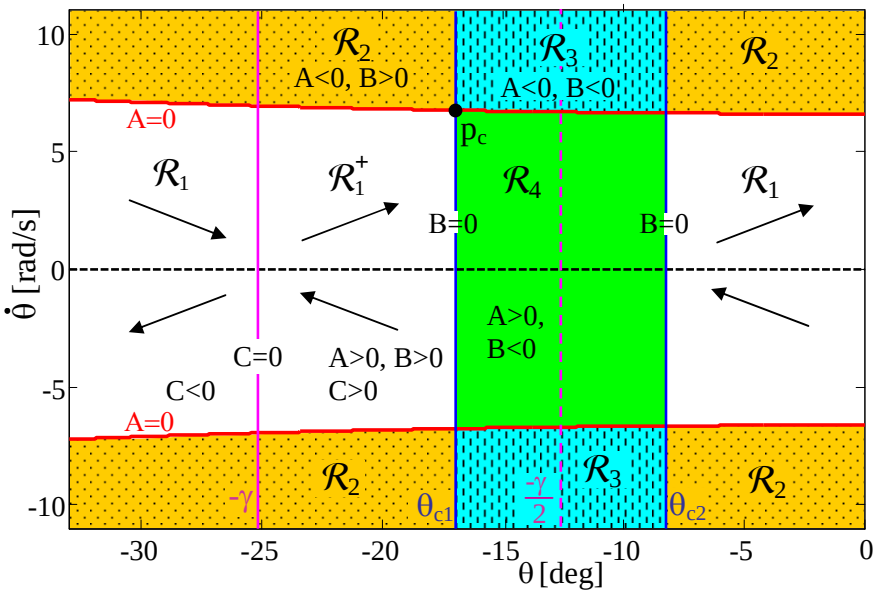

Fig. 5 Partition of the $(\theta, \dot{\theta})$-plane into regions according to the sign of A, B, and C.

Parameter	Physical Value
l	300 mm
e	10 mm
r_1	60 mm
r_2	200 mm
m_1	0.15 Kg
m_2	5.0 Kg
ρ_1	85.0 mm
ρ_2	25.0 mm
h	12 mm
α	30°

Table 4 Physical values for the IPOS parameters.

As a concrete example, consider the specific values for the IPOS parameters in Table 4. When these values are substituted into (18), $\mu_{min} = 0.44$. Any $\mu > 0.44$ is associated with the existence of solution inconsistency where $B(\theta, \mu) < 0$. For instance, when $\mu = 0.47$ the critical angles are $\theta_{c1} = -16.94°$ and $\theta_{c2} = -8.23°$, and $B(\theta, \mu) < 0$ in the interval $[-16.94°, -8.23°]$.

4.2 IPOS Phase Plane Trajectories

We now analyze the solutions of the IPOS mechanism during a consistent sliding motion which approaches the inconsistency region with $B(\theta(t), \mu) \to 0$. The dynamics of IPOS depends only on the hinge angle and velocity, $(\theta, \dot{\theta})$. Hence we analyze the behavior of solution trajectories in the phase plane $(\theta, \dot{\theta})$. The following lemma, whose proof appears in the appendix, specifies the IPOS dynamics in the phase plane $(\theta, \dot{\theta})$.

Lemma 4.1 *The dynamics of the IPOS hinge angle θ is given by*

$$\ddot{\theta} = C(\theta, \mu) \frac{A(\theta, \dot{\theta})}{B(\theta, \mu)}, \tag{19}$$

where $A(\theta, \dot{\theta})$ and $B(\theta, \mu)$ are defined in (12), and

$$C(\theta, \mu) = \frac{\sqrt{1 + \mu^2}}{m_{eq} r_{eq}} \sin(\theta + \gamma). \tag{20}$$

Note that (19) is a singular ODE. This particular type of singularity, which is precisely the mathematical origin of Painlevé's paradox, cannot be analyzed by using Filippov-like treatment (cf. [9]) since the solutions do not attain the singularity surface $B(\theta, \mu) = 0$ in a transversal manner, as will be shown in the sequel. Figure 5 shows a partition of the phase plane $(\theta, \dot{\theta})$ into regions according to the sign of A, B, and C, for the parameter values specified in Table 4 and coefficient of friction $\mu = 0.47$. As originally presented in [10], this plot provides useful information about the behavior of solution trajectories of the IPOS dynamics. The regions $\mathcal{R}_1$, $\mathcal{R}_2$, $\mathcal{R}_3$, and $\mathcal{R}_4$ correspond to cases 1, 2, 3, and 4 of Table 1. In particular, $\mathcal{R}_1$ corresponds to consistent sliding while $\mathcal{R}_4$ corresponds to solution inconsistency. The locus of $B(\theta, \mu) = 0$ is the two vertical lines $\theta = \theta_{c1}$ and $\theta = \theta_{c2}$. The locus of $A(\theta, \dot{\theta}) = 0$ is the two nearly-horizontal parabolic curves indicated in the figure. The locus of $C(\theta, \mu) = 0$ is the vertical line $\theta = -\gamma$. The inconsistency region, $\mathcal{R}_4$, lies within the vertical strip spanned by the interval $\theta \in [\theta_{c1}, \theta_{c2}]$, between the pseudo-parabolic curves corresponding to $A(\theta, \dot{\theta}) = 0$. The arrows in Figure 5 show typical directions of the local tangent, $(\ddot{\theta}, \dot{\theta})$, to solution curves

$(\theta(t), \dot\theta(t))$ of (19). As indicated by the arrows, the only way for a consistent sliding solution with zero initial velocity, $\dot\theta(0) = 0$, to reach $\mathcal{R}_4$ is by approaching the vertical line $\theta = \theta_{c1}$ from its left side. This gives the dynamic jamming scenario which is next considered.

4.3 IPOS Dynamic Jamming Trajectories

Consider a consistent sliding solution, $(\theta(t), \dot\theta(t))$, which starts in the region $\mathcal{R}_1$ and approaches the vertical line $\theta = \theta_{c1}$, so that $B(\theta(t), \mu) \to 0$ along this solution. During this motion $a_n = 0$ while $f_n > 0$. The governing equation takes the form $0 = -A(\theta, \dot\theta) + B(\theta, \mu) f_n$, and f_n is given by $f_n = A(\theta, \dot\theta)/B(\theta, \mu)$. It is tempting to conclude that f_n grows unbounded as $B(\theta, \mu) \to 0$. However, this is not necessarily the case, as we now show.

The following analysis extends the results presented for Painlevé's sliding rod example in [10]. Consider initial conditions lying in the region $\mathcal{R}_1^+$, defined as

$$\mathcal{R}_1^+ = \{(\theta, \dot\theta) : \ -\gamma < \theta < \theta_{c1} \\ \text{and } \dot\theta > 0 \text{ and } A(\theta, \dot\theta) > 0\}.$$

The region $\mathcal{R}_1^+$ is the subset of $\mathcal{R}_1$ delineated by the inequalities $A(\theta, \dot\theta) > 0$, $B(\theta, \mu) > 0$, and $C(\theta, \mu) > 0$. It is bounded from above by the curve $A(\theta, \dot\theta) = 0$, on the left by the vertical line $\theta = -\gamma$, and on the right by the vertical line $\theta = \theta_{c1}$ (Figure 5). The following lemma states that solutions of (19) starting in $\mathcal{R}_1^+$ *cannot* reach the vertical line $\theta = \theta_{c1}$ *before* reaching the curve $A(\theta, \dot\theta) = 0$.

Lemma 4.2 *Let $(\theta(t), \dot\theta(t))$ be a solution of the IPOS dynamical equation (19) with initial condition $(\theta(0), \dot\theta(0)) \in \mathcal{R}_1^+$. There exists a finite time, $t_A > 0$, such that $A(\theta(t_A), \dot\theta(t_A)) = 0$ while $B(\theta(t), \mu) > 0$ for all $t \in [0, t_A)$.*

Note that the since the time interval is open at t_A, the lemma still allows the possibility that a solution $(\theta(t), \dot\theta(t))$ will start in $\mathcal{R}_1^+$ and reach the corner point where both $A(\theta, \dot\theta)$ and $B(\theta, \mu)$ vanish simultaneously at the time $t = t_A$.

Proof: The proof follows the steps given in [10] for Painlevé's rod, with the required extensions and a slightly different interpretation. By construction $A(\theta, \dot\theta)$, $B(\theta, \mu)$, and $C(\theta, \mu)$ are strictly positive in $\mathcal{R}_1^+$. Since $\ddot\theta = C(\theta, \mu) A(\theta, \dot\theta)/B(\theta, \mu)$ according to (19), $\ddot\theta$ is strictly positive in $\mathcal{R}_1^+$. Since $\dot\theta$ is also strictly positive in $\mathcal{R}_1^+$, $\theta(t)$ and $\dot\theta(t)$ are monotonically increasing with t along solutions of (19) in $\mathcal{R}_1^+$. In particular, $\theta(t)$ is strictly increasing with $\dot\theta(t) \geq \dot\theta(0) > 0$. Hence every solution either reaches the vertical line $\theta = \theta_{c1}$ where $B(\theta, \mu) = 0$ in finite time, or reaches the curve $A(\theta, \dot\theta) = 0$ at an earlier time. Assume, by contradiction, that there exists a solution $(\theta(t), \dot\theta(t))$ which reaches $B(\theta, \mu) = 0$ *before* reaching $A(\theta, \dot\theta) = 0$. That is, assume that there exists a finite time $t_B > 0$ such that $B(\theta(t_B), \mu) = 0$ while $A(\theta(t), \dot\theta(t)) > 0$ for all $t \in [0, t_B]$. In this case there exists $K_A > 0$ such that $A(\theta(t), \dot\theta(t)) > K_A$ for $t \in [0, t_B]$. According to (20), $C(\theta, \mu) = c \sin(\theta + \gamma)$ where $c > 0$. Since $\theta(t)$ is monotonically increasing with t and $\sin(\theta + \gamma)$ is monotonically increasing with θ in $\mathcal{R}_1^+$, $C(\theta(t), \mu)$ is monotonically increasing with t for $t \in [0, t_B]$. Denoting $K_C = C(\theta(0), \mu) > 0$, we have that $C(\theta(t), \mu) \geq K_C$ for all $t \in [0, t_B]$. Using these bounds and the dynamic equation (19), $\ddot\theta \geq K_A K_C / B(\theta(t), \mu)$ for $t \in [0, t_B]$. Since $\theta(t)$ is monotonically increasing with t, we may choose a new time-scale given by $\bar t = \theta(t)$. Let $\omega(t) = \dot\theta(t)$ and let $\bar\omega(\bar t) = \omega(\theta^{-1}(\bar t))$. The derivative of $\bar\omega$ with respect to $\bar t$ is given by

$$\frac{d\bar\omega(\bar t)}{d\bar t} = \frac{d\omega}{dt} \cdot \frac{d\theta^{-1}(\bar t)}{d\bar t} = \frac{d\omega/dt}{d\bar t/dt} = \frac{\ddot\theta(\theta = \bar t, \dot\theta = \omega(\theta^{-1}(\bar t)))}{\bar\omega(\bar t)}. \tag{21}$$

The intuitive meaning of this rescaling is that θ is used as the independent parameter defining solution curves in $(\theta, \dot\theta)$ plane, and the derivative $d\bar\omega/d\bar t$ is simply the *slope* of local tangent to a solution curve. Using the lower bounds K_A and K_C, we arrive at

$$\frac{d\bar\omega(\bar t)}{d\bar t} \geq \frac{K_A K_C}{\bar\omega(\bar t) B(\bar t, \mu)},$$

where B is specified in (20). Using separation of variables and integrating, we obtain

$$\frac{\bar\omega^2(\bar t)}{2} = \int \bar\omega d\bar\omega \geq \int \frac{K_A K_C}{B(\bar t, \mu)} d\bar t \\ = \frac{m_{eq} K_A K_C}{\sqrt{1 + \mu^2 - \kappa^2}} \operatorname{arctanh}\left(\frac{(\kappa + \sqrt{1 + \mu^2}) \tan(\bar t + \frac{\gamma}{2})}{\sqrt{1 + \mu^2 - \kappa^2}} \right). \tag{22}$$

The function $\operatorname{arctanh}(x)$ is defined in the interval $-1 \leq x \leq 1$, and $\operatorname{arctanh}(x) \to \pm\infty$ as $x \to \pm 1$. Using formula (18) for θ_{c1} and some trigonometric manipulations, it can be verified that the argument of $\operatorname{arctanh}(\cdot)$ in (22) approaches unity as $\bar t \to \theta_{c1}$. The right side of (22) thus diverges to infinity as $\bar t \to \theta_{c1}$. Since $\bar t = \theta(t)$ and $\bar\omega(\bar t) = \dot\theta(t)$, $\dot\theta(t)$ diverges to infinity while $\theta(t)$ approaches the vertical line $\theta = \theta_{c1}$ as $t \to t_B$. This leads to a contradiction, since the $\dot\theta$ coordinate of points $(\theta, \dot\theta) \in \mathcal{R}_1^+$ is bounded from above by the curve $A(\theta, \dot\theta) = 0$. □

When a consistent sliding trajectory approaches the curve $A(\theta,\dot\theta)=0$ away from the vertical line $\theta=\theta_{c1}$, the normal contact force f_n vanishes, leading to separation of the slider from the inclined plane. However, Lemma 4.2 also allows the possibility of solutions reaching at time $t=t_A$ the point where $\theta=\theta_{c1}$ and $A(\theta_{c1},\dot\theta)=0$. We define the critical *corner point* as the point $p_c=(\theta_{c1},\dot\theta_{c1})$, where $\dot\theta_{c1}$ is the positive root of $A(\theta_{c1},\dot\theta_{c1})=0$ (Figure 5). The behavior of solution trajectories in vicinity of the critical corner point p_c is next considered.

4.4 IPOS Solutions in the Vicinity of p_c

This section analyzes the IPOS trajectories in the vicinity of the critical corner point p_c. The approach taken here focuses on the eigenvectors of the linearized dynamics, and thus complements the algebraic approach taken in [10] for Painlevé's sliding rod example. Since $B(\theta,\mu)$ is strictly positive in the region of interest $\mathcal{R}_1^+$, we follow [10] and define the time transformation $s(t)=\int_{t'=0}^{t}\frac{1}{B(\theta(t'),\mu)}dt'$. In the new time, s, the singularity $B\to 0$ is approached only *asymptotically* as $s\to\infty$. Setting $x_1=\theta$ and $x_2=\dot\theta$, the dynamics (19) can be written as ([10]):

$$\begin{aligned}\frac{dx_1}{ds}&=B(x_1,\mu)x_2\\ \frac{dx_2}{ds}&=C(x_1,\mu)A(x_1,x_2)\end{aligned}\tag{23}$$

Since A and B vanish at p_c, the critical corner point is an equilibrium point of (23). The dynamic behavior of (23) in the vicinity of p_c is governed by its *linearization* at p_c. Recall that $p_c=(\theta_{c1},\dot\theta_{c1})$, where $\dot\theta_{c1}$ is the positive root of $A(\theta_{c1},\dot\theta_{c1})=0$. Denoting $Y=(\theta-\theta_{c1},\ \dot\theta-\dot\theta_{c1})$, the linearized dynamics of (23) at p_c is given by

$$\frac{d}{ds}Y(s)=\begin{bmatrix}\alpha_1 & 0\\ \alpha_2 & \alpha_3\end{bmatrix}Y(s)\tag{24}$$

where

$$\begin{aligned}\alpha_1&=\frac{\partial B}{\partial\theta}(\theta_{c1},\mu)\dot\theta_{c1}=\frac{\sqrt{1+\mu^2}}{m_{eq}}\dot\theta_{c1}\sin(2\theta_{c1}+\gamma)\\ \alpha_2&=C(\theta_{c1},\mu)\frac{\partial A}{\partial\theta}(\theta_{c1},\dot\theta_{c1})=\frac{\sqrt{1+\mu^2}}{m_{eq}}\dot\theta_{c1}^2\sin(\theta_{c1}+\gamma)\sin(\theta_{c1})\\ \alpha_3&=C(\theta_{c1},\mu)\frac{\partial A}{\partial\dot\theta}(\theta_{c1},\dot\theta_{c1})=-2\frac{\sqrt{1+\mu^2}}{m_{eq}}\dot\theta_{c1}\sin(\theta_{c1}+\gamma)\cos(\theta_{c1}).\end{aligned}\tag{25}$$

The eigenvalues of the linearization matrix in (24), denoted λ_1 and λ_2, are the real scalars $\lambda_1=\alpha_1$ and $\lambda_2=\alpha_3$. The corresponding eigenvectors are $\boldsymbol{v}_1=(\alpha_1-\alpha_3,\alpha_2)$ and $\boldsymbol{v}_2=(0,1)$. Since θ_{c1} lies in the interval $[-\gamma,-\gamma/2]$ (Figure 5), $\sin(2\theta_{c1}+\gamma)<0$ and $\sin(\theta_{c1}+\gamma)\cos(\theta_{c1})>0$. The eigenvalues are therefore negative, and p_c is *locally asymptotically stable*. However, when a solution trajectory crosses the curve $A(\theta,\dot\theta)=0$ while approaching p_c, the contact force vanishes and the dynamics (23) no longer holds true. Therefore, the way in which trajectories converge to p_c has a significant influence on the dynamic behavior, as we now show.

The local tangent to the curve $A(\theta,\dot\theta)=0$ at p_c is given by $\boldsymbol{u}=(\alpha_3,-\alpha_2)$. Since α_2 and α_3 are both negative in $\mathcal{R}_1^+$, $\boldsymbol{u}$ lies in the $(-,+)$ quadrant of the $(\theta,\dot\theta)$ plane (Figure 6). The general form of a solution to (24) is given by $Y(s)=c_1\boldsymbol{v}_1\exp(\lambda_1 s)+c_2\boldsymbol{v}_2\exp(\lambda_2 s)$, where the scalars c_1,c_2 are determined by the initial conditions. There are two qualitatively distinct cases which depend on the relation between λ_1 and λ_2. First consider the case where $\lambda_1>\lambda_2$. In this case solution trajectories of (24) start in parallel to $\boldsymbol{v}_2$ (the vertical axis), then converge to p_c along the eigenvector $\boldsymbol{v}_1$ as shown in Figure 6(a). In this case the eigenvector $\boldsymbol{v}_1$ lies in the $(-,+)$ quadrant of the $(\theta,\dot\theta)$ plane, which is also occupied by the local tangent $\boldsymbol{u}$. The local tangent can be written as $\boldsymbol{u}=\boldsymbol{v}_1+\binom{\alpha_1}{0}$. Since α_1 is negative, $\boldsymbol{u}$ lies *below* the eigenvector $\boldsymbol{v}_1$ (Figure 6(a)). It is clear from the figure that all possible trajectories cross the curve $A(\theta,\dot\theta)=0$ *before* reaching p_c. At this instant the contact force vanishes, leading to contact separation, so that (24) ceases to hold.

Next consider the case where $\lambda_1<\lambda_2$. In this case solution trajectories of (24) start in parallel to $\boldsymbol{v}_1$, then converge to p_c along the eigenvector $\boldsymbol{v}_2$ (the vertical axis), as shown in Figure 6(b). The eigenvector $\boldsymbol{v}_1$ now lies in the $(-,-)$ quadrant of the $(\theta,\dot\theta)$ plane. Solutions starting above the line of $\boldsymbol{v}_1$ cross the curve $A(\theta,\dot\theta)=0$ before reaching p_c. However, the local tangent $\boldsymbol{u}$ now lies *above* $\boldsymbol{v}_1$. Hence solutions starting below the line of $\boldsymbol{v}_1$ converge to p_c along the vertical axis without crossing the curve $A(\theta,\dot\theta)=0$. Rigorous analysis of the limit of the normal contact force, $f_n=A(x_1,x_2)/B(x_1,\mu)$ as $(x_1,x_2)\to p_c$, shows that in this case f_n *diverges to infinity*, as B tends asymptotically to zero faster than A [10]. Some insight into this behavior can be gained from the following argument. Since A and B vanish at p_c, their first-order approximation in the vicinity of this point is given by $A\cong\nabla A\cdot Y$ and $B\cong\nabla B\cdot Y$, where the gradient vectors are evaluated at p_c. Substituting the solution $Y(s)=c_1\boldsymbol{v}_1\exp(\lambda_1 s)+c_2\boldsymbol{v}_2\exp(\lambda_2 s)$ gives the following ex-

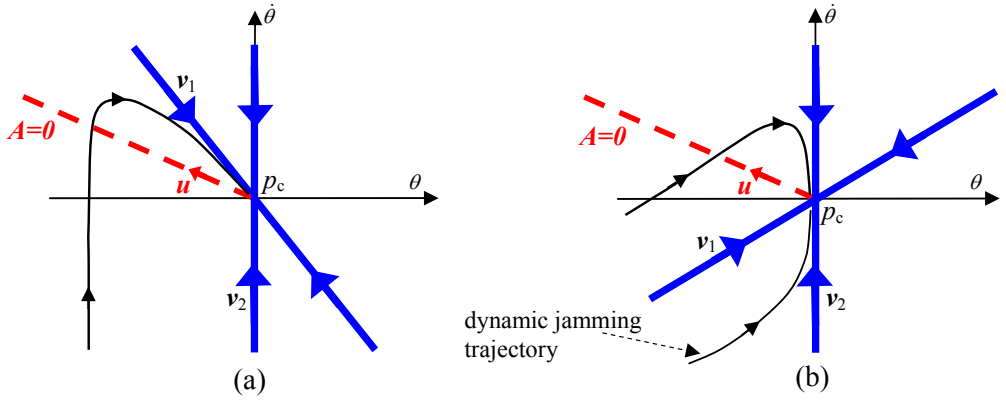

Fig. 6 Sketch of the IPOS linearized dynamics at p_c and typical solution trajectories for (a) $\lambda_2 < \lambda_1$, and (b) $\lambda_2 > \lambda_1$.

pression for the normal force,

$$f_n(s) = \frac{A(s)}{B(s)} \approx \frac{a_1 e^{\lambda_1 s} + a_2 e^{\lambda_2 s}}{b_1 e^{\lambda_1 s} + b_2 e^{\lambda_2 s}},$$

where $a_i = c_i \nabla A \cdot \boldsymbol{v}_i$ and $b_i = c_i \nabla B \cdot \boldsymbol{v}_i$ for $i = 1, 2$. Since B is independent of $\dot\theta$, ∇B is orthogonal to the eigenvector $\boldsymbol{v}_2$, so that $b_2 = 0$. Hence $f_n(s) \cong \frac{a_1}{b_1} + \frac{a_2}{b_1} e^{(\lambda_2 - \lambda_1)s}$. Since $\lambda_2 - \lambda_1 > 0$, $|f_n(s)| \to \infty$ as $s \to \infty$. Finally, it can be verified that $a_2/b_1 > 0$. Hence f_n diverges to $+\infty$ as $s \to \infty$.

The condition $\lambda_1 < \lambda_2$ can be written as the following lower bound on the friction coefficient.

Proposition 4.3 *Consider the linearized dynamics of the IPOS mechanism, eq. (24), at the critical corner point p_c. When the friction coefficient satisfies $\mu > \mu_c$ where μ_c is given by*

$$\mu_c = \frac{2}{\sqrt{3}} \mu_{min} = \frac{2}{\sqrt{3}} \sqrt{\kappa^2 - 1}, \tag{26}$$

and κ is given in (17), there exist solution trajectories that approach p_c with unbounded normal contact force f_n.

Proof: The condition for the existence of solutions with f_n growing unbounded in finite time, $\lambda_1 < \lambda_2$, can be written as $\alpha_1 < \alpha_3$. Substituting for α_1 and α_3 according to (25), then using the fact that m_{eq} and $\dot\theta_{c1}$ are positive, gives the equivalent condition:

$$\sin(2\theta_{c1} + \gamma) + 2\sin(\theta_{c1} + \gamma)\cos(\theta_{c1}) < 0. \tag{27}$$

Using trigonometric manipulations, (27) can be written as

$$2\sin(2\theta_{c1} + \gamma) + \sin\gamma < 0. \tag{28}$$

Substituting for θ_{c1} according to (18) and using the relation $\mu = \tan\gamma$, one obtains

$$\sin(2\theta_{c1} + \gamma) = -\sqrt{1 - \cos(2\theta_{c1} + \gamma)} = -\sqrt{\frac{1 + \mu^2 - \kappa^2}{1 + \mu^2}}.$$

Substituting for $\sin(2\theta_{c1} + \gamma)$ and $\sin\gamma = \mu/\sqrt{1 + \mu^2}$ into (28) gives $2\sqrt{1 + \mu^2 - \kappa^2} > \mu$. Taking the square of both sides gives $3\mu^2 - 4(\kappa^2 - 1) > 0$, which finally leads to (26). □

Let us make some remarks on the linearized dynamics and the lower bound μ_c. First, it can be verified that the eigenvector $\boldsymbol{v}_1$ rotates in clockwise direction as μ increases. Therefore, the region of initial conditions leading to an unbounded contact force (and hence dynamic jamming) becomes larger as μ increases. Second, in the case of a rod with uniform mass distribution under a point contact, substituting $m_1 = 0$ and $\rho_2^2 = r_2^2/3$ into μ_{min} gives $\mu_c = 8/(3\sqrt{3})$, which is precisely the critical value obtained in [10] for Painlevé's rod example. Last, when the specific values of m_1, m_2, r_2, and ρ_2 from Table 4 are substituted into (26), the critical value for μ in the IPOS mechanism is $\mu_c = 0.51$.

The following theorem summarizes the results of this section in terms of three intervals of μ, which give three distinct behaviors of the IPOS sliding trajectories.

Theorem 1 *Consider the IPOS dynamics (19) under forward sliding motion with $\dot x(t) > 0$. When $\mu \le \mu_{min}$, all solutions that start in $\mathcal{R}_1^+$ either keep sliding or undergo contact separation. When $\mu_{min} < \mu \le \mu_c$, there exists an interval $\theta \in (\theta_{c1}, \theta_{c2})$ corresponding to solution inconsistency. In this case all solutions that start in $\mathcal{R}_1^+$ undergo contact separation before reaching solution inconsistency. When $\mu > \mu_c$, there exists a region of initial conditions in $\mathcal{R}_1^+$ whose solutions reach the critical corner point p_c where the normal contact force f_n becomes unbounded and the mechanism undergoes dynamic jamming.*

Dynamic jamming can thus occur only when $\mu > \mu_c$. In this case a trajectory can reach in finite time the critical corner point p_c where f_n grows unbounded. The dynamics of the mechanism's x coordinate, considered in the next section, indicates that $\ddot x \to -\infty$

as the solution approaches p_c. The scenario of dynamic jamming thus involves an abrupt halting of the sliding motion (a tangential impact or impact without collision), which is followed by contact separation.

5 Conditions for Maintaining IPOS Sliding Motion Toward Dynamic Jamming

The existence of dynamic jamming trajectories in the IPOS mechanism is based on two assumptions. The mechanism is assumed to keep its forward sliding motion until dynamic jamming is reached, and to maintain line contact with the inclined plane during its forward sliding motion. This section derives conditions under which the mechanism satisfies these two assumptions. These conditions will guide our choice of initial conditions for the IPOS trajectories simulated in the next section.

5.1 A Sufficient Condition for Maintaining IPOS Sliding Motion

The IPOS mechanism is required to maintain its forward sliding motion, $\dot{x} > 0$, during the time interval leading to dynamic jamming. Since the mechanism's tangential sliding velocity $\dot{x}$ decreases during this time interval, the mechanism may experience transition to tangential sticking of the slider before reaching dynamic jamming. Hence we derive a lower bound on the mechanism's initial sliding velocity, $\dot{x}(0)$, guaranteeing that no tangential sticking will occur before the critical corner point p_c is reached. While the *existence* of such a bound is mentioned in [10] for Painlevé's sliding rod example, its explicit computation is a contribution of this paper.

Using the mechanism's full dynamic equation (10) with the expressions (11) and (14), the dynamics of its x coordinate is obtained as

$$\ddot{x} = \frac{C_x(\theta,\mu)A(\theta,\dot{\theta})}{B(\theta,\mu)} + D_x(\theta,\dot{\theta}) \tag{29}$$

where C_x and D_x are given by

$$\begin{aligned} C_x(\theta,\mu) &= -r_{eq}\cos\theta \cdot C(\theta,\mu) - \frac{\mu(r_2 r_{eq}+\rho_2^2)}{m_1(r_2^2+\rho_2^2)+m_2\rho_2^2} \\ D_x(\theta,\dot{\theta}) &= r_{eq}\dot{\theta}^2\sin\theta + g\sin\alpha, \end{aligned} \tag{30}$$

and $A(\theta,\dot{\theta})$, $B(\theta,\mu)$, and $C(\theta,\mu)$ are given in (20). The following lemma specifies a lower bound on $\dot{x}(0)$ guaranteeing that the IPOS mechanism will maintain its forward sliding motion up to the dynamic jamming event.

Lemma 5.1 *Let the IPOS mechanism start sliding on an inclined plane with slope angle α, with $(\theta(0),\dot{\theta}(0)) \in \mathcal{R}_1^+$ such that $\theta(0) > -\alpha$. Let θ_{c1} be the hinge coordinate at the critical corner point p_c. If $\dot{x}(0)$ satisfies the lower bound*

$$\dot{x}(0) > |c|\left(\sqrt{\frac{g\cos\alpha}{r_{eq}\cos(\theta(0))}} - \dot{\theta}(0)\right) \qquad c = \frac{C_x(\theta_{c1},\mu)}{C(\theta_{c1},\mu)}, \tag{31}$$

there exists a finite time $t_A > 0$ at which $A(\theta(t_A),\dot{\theta}(t_A)) = 0$ while $\dot{x}(t) > 0$ for all $t \in [0, t_A]$.

The critical corner point, p_c, is located on the curve $A(\theta,\dot{\theta}) = 0$. Hence a dynamic jamming trajectory starting with $\dot{x}(0)$ satisfying (31) is guaranteed to reach p_c without any tangential sticking. Note that the condition $\theta(0) > -\alpha$ is automatically satisfied when $\alpha > \gamma$ i.e., when the inclined plane angle α is steeper than the friction cone half-angle γ (this observation follows from the fact that $\theta(0) > -\gamma$ in $\mathcal{R}_1^+$, hence $\alpha > \gamma$ implies $\theta(0) > -\alpha$).

Proof: Recall that $\dot{\theta}(t)$ is monotonically increasing with t along solutions of (19) in $\mathcal{R}_1^+$. One can therefore introduce the time transformation $s = \dot{\theta}(t)$, which would allow us to assess the relative changes in $\dot{x}$ and $\dot{\theta}$ along solution trajectories. The derivative of $\dot{x}$ with respect to s is given by

$$\frac{d\dot{x}(s)}{ds} = \frac{d\dot{x}/dt}{ds/dt} = \frac{\ddot{x}}{\ddot{\theta}}. \tag{32}$$

According to Lemma 4.2, there exists a finite time $t_A > 0$ at which the solution of (19) satisfies $A(\theta(t_A),\dot{\theta}(t_A)) = 0$ (in particular, $\theta(t_A) = \theta_{c1}$ along a dynamic jamming trajectory). Let the interval $s \in [s_0, s_1]$ correspond to the time interval $t \in [0, t_A]$ i.e., $s_0 = \dot{\theta}(0)$ and $s_1 = \dot{\theta}(t_A)$. Substituting the expressions for $\ddot{\theta}$ and $\ddot{x}$ from (19) and (29) into (32) gives

$$\frac{d\dot{x}(s)}{ds} = \frac{C_x(\theta,\mu)A(\theta,\dot{\theta}) + B(\theta,\mu)D_x(\theta,\dot{\theta})}{C(\theta,\mu)A(\theta,\dot{\theta})} \tag{33}$$

for $s \in [s_0, s_1]$, where C_x and D_x are specified in (30) while A, B, and C are specified in (12) and (20).

Since $A(\theta,\dot{\theta}) = g\cos\alpha - r_{eq}\dot{\theta}^2\cos\theta$, one obtains $\frac{\partial A}{\partial\theta}(\theta,\dot{\theta}) = r_{eq}\dot{\theta}^2\sin\theta < 0$ and $\frac{\partial A(\theta,\dot{\theta})}{\partial\dot{\theta}} = -2r_{eq}\dot{\theta}\cos\theta < 0$ for all $(\theta,\dot{\theta}) \in \mathcal{R}_1^+$, where we used the facts that $\sin\theta < 0$, $\cos\theta > 0$, and $\dot{\theta} \geq 0$ in $\mathcal{R}_1^+$. Consider the intersection point of the vertical line passing through $(\theta(0),\dot{\theta}(0))$ and the curve $A(\theta,\dot{\theta}) = 0$ which forms the upper boundary of $\mathcal{R}_1^+$. The $\dot{\theta}$ coordinate of this point, ω_0, is given by

$$\omega_0 = \sqrt{\frac{g\cos\alpha}{r_{eq}\cos(\theta(0))}}.$$

We now show that $\dot{\theta}(t_A) < \omega_0$. Since $\theta(t)$ is monotonically increasing with t, $\theta(t_A) > \theta(0)$. Since $A(\theta(0), \omega_0) = 0$ and $\partial A/\partial\theta < 0$, the relation $\theta(t_A) > \theta(0)$ implies that $A(\theta(t_A), \omega_0) < 0$. The points $(\theta(t_A), \dot{\theta}(t_A))$ and $(\theta(t_A), \omega_0)$ share the same θ coordinate. Since $\partial A/\partial\dot{\theta} < 0$, the fact that $A(\theta(t_A), \dot{\theta}(t_A)) = 0$ and $A(\theta(t_A), \omega_0) < 0$ implies that $\dot{\theta}(t_A) < \omega_0$.

We now obtain a lower bound on $d\dot{x}(s)/ds$ in (33). Using the expression for $A(\theta, \dot{\theta})$ and the fact that $A(\theta, \dot{\theta}) \geq 0$ in $\mathcal{R}_1^+$,

$$\dot{\theta}^2 \leq \frac{g\cos\alpha}{r_{eq}\cos\theta} \qquad \text{for all } (\theta, \dot{\theta}) \in \mathcal{R}_1^+.$$

Consider the term $D_x(\theta, \dot{\theta}) = r_{eq}\dot{\theta}^2 \sin\theta + g\sin\alpha$. Using the upper bound on $\dot{\theta}^2$ and the fact that $\sin\theta < 0$ in $\mathcal{R}_1^+$,

$$D_x(\theta, \dot{\theta}) \geq g\cos\alpha(\tan\theta + \tan\alpha) \quad \text{for all } (\theta, \dot{\theta}) \in \mathcal{R}_1^+. \tag{34}$$

By assumption $\theta(0) > -\alpha$. Hence $\tan(\theta(0)) + \tan\alpha > 0$. Since $\tan(\theta(t))$ is monotonically increasing with t, (34) implies that D_x is lower bounded by

$$D_x(\theta(t), \dot{\theta}(t)) \geq g\cos\alpha(\tan(\theta(0)) + \tan\alpha) > 0$$

for $t \in [0, t_A]$. Since $A, B, C \geq 0$ in $\mathcal{R}_1^+$ and $D_x > 0$, (33) implies that

$$\frac{d\dot{x}(s)}{ds} > \frac{C_x(\theta(s), \mu)}{C(\theta(s), \mu)} \qquad \text{for } s \in [s_0, s_1].$$

The fraction $C_x(\theta, \mu)/C(\theta, \mu)$ is monotonically decreasing with θ in the interval $\theta \in [-\gamma, \theta_{c1}]$. Since $\theta(s)$ is monotonically increasing with s, the fraction $C_x(\theta(s), \mu)/C(\theta(s), \mu)$ is monotonically decreasing with s and therefore lower bounded by

$$\frac{C_x(\theta(s), \mu)}{C(\theta(s), \mu)} \geq \frac{C_x(\theta(s_1), \mu)}{C(\theta(s_1), \mu)} \qquad \text{for } s \in [s_0, s_1].$$

Substituting $\theta(s_1) = \theta(t_A) = \theta_{c1}$, one obtains the lower bound

$$\frac{d\dot{x}(s)}{ds} > \frac{C_x(\theta_{c1}, \mu)}{C(\theta_{c1}, \mu)} \qquad \text{for } s \in [s_0, s_1].$$

Define $c = C_x(\theta_{c1}, \mu)/C(\theta_{c1}, \mu)$. Since $d\dot{x}(s)/ds$ is lower bounded by c,

$$\dot{x}(s) > \dot{x}(s_0) + c(s - s_0) \qquad \text{for } s \in [s_0, s_1]\ .$$

Substituting $s_0 = \dot{\theta}(0)$ and $s = \dot{\theta}(t)$ gives

$$\dot{x}(t) > \dot{x}(0) + c\big(\dot{\theta}(t) - \dot{\theta}(0)\big) \qquad \text{for } t \in [0, t_A].$$

The sign of $c = C_x(\theta_{c1}, \mu)/C(\theta_{c1}, \mu)$ is negative, since $C(\theta_{c1}, \mu) > 0$ while $C_x(\theta_{c1}, \mu) < 0$. Since $c < 0$ and $\dot{\theta}(t) < \omega_0$,

$$\dot{x}(t) > \dot{x}(0) + c(\omega_0 - \dot{\theta}(0)) \quad \text{for } t \in [0, t_A].$$

The condition $\dot{x}(0) + c(\omega_0 - \dot{\theta}(0)) > 0$ implies that $\dot{x}(t) > 0$ for $t \in [0, t_A]$, and this is precisely condition (31) of the lemma. □

5.2 A Sufficient Condition for Maintaining IPOS Line Contact

The IPOS mechanism is also required to maintain line contact with the inclined plane, $\psi = 0$, during the time interval leading to dynamic jamming. As discussed in Section 3, the normal reaction force distribution can be lumped into a single normal force acting on the slider at a point $\boldsymbol{x} \in P$. As long as $\boldsymbol{x}$ lies within the contact segment, the net torque generated by the normal reaction force distribution, τ, is able to maintain the slider's orientation at $\psi = 0$ (and hence the line contact). Based on (13), the point $\boldsymbol{x}$ lies within the contact segment when it satisfies the inequalities:

$$-\frac{l}{2} \leq \frac{\tau}{f_n} + r_1 \leq \frac{l}{2},$$

where l is the slider's length and r_1 is the distance of the slider's origin from its geometric center. The net torque τ is specified in (14) as

$$\tau(\theta, \dot{\theta}) = C_\tau(\theta, \mu) f_n + D_\tau(\theta, \dot{\theta}),$$

where C_τ and D_τ are listed in (15). The line contact condition is thus

$$-\frac{l}{2} \leq C_\tau(\theta, \mu) + \frac{D_\tau(\theta, \dot{\theta})}{f_n(\theta, \dot{\theta})} + r_1 \leq \frac{l}{2}. \tag{35}$$

We derive a lower bound on the slider's length, l, such that (35) will hold true during the time interval leading to dynamic jamming. Since the normal reaction force, f_n, appears in the denominator of (35), we need to lower bound f_n along dynamic jamming trajectories. The proof of the following lemma appears in the appendix.

Lemma 5.2 *Let the IPOS mechanism start sliding with $(\theta(0), \dot{\theta}(0)) \in \mathcal{R}_1^+$ and reach the critical corner point $p_c = (\theta_{c1}, \dot{\theta}_{c1})$ at $t = t_A$. The normal reaction force along this trajectory satisfies the lower bound*

$$f_n(t) \geq \frac{1}{\mu} m_{eq} g\cos\alpha\,|\tan(\theta_{c1})| \quad \textit{for } t \in [0, t_A],$$

where $\mu > \mu_c$ is the friction coefficient and α is the inclined plane slope angle.

Let us assume for simplicity that the mechanism's hinge is mounted above the slider's center, so that $r_1 = 0$ in the IPOS mechanism. The following proposition provides a lower bound on the slider's length which maintains line contact along dynamic jamming trajectories.

Proposition 5.3 *Let the IPOS mechanism start sliding with* $(\theta(0),\dot\theta(0))\in\mathcal{R}_1^+$ *and reach the critical corner point* $p_c=(\theta_{c1},\dot\theta_{c1})$ *at* $t=t_A$. *The slider maintains line contact with the inclined plane for* $t\in[0,t_A]$ *when its length is lower bounded by*

$$l\geq 2\left(\max\{C_\tau(-\gamma,\mu),C_\tau(\theta_{c1},\mu)\}+\frac{m_1r_{eq}\dot\theta_{c1}^2\sin\gamma}{f_n^0}\right)$$
$$f_n^0=\tfrac{1}{\mu}m_{eq}g\cos\alpha\,|\tan(\theta_{c1})|,$$

where $C_\tau(\theta,\mu) = \mu\big(e-2m_2h/(m_1+m_2)\big) + m_1h\sqrt{1+\mu^2}\sin(\theta+\gamma)\cos\theta/m_{eq}$.

Proof: Under the $r_1=0$ assumption, the slider maintains line contact when its length l satisfies the inequalities:

$$-\frac{l}{2}\leq C_\tau(\theta,\mu)+\frac{D_\tau(\theta,\dot\theta)}{f_n(\theta,\dot\theta)}\leq\frac{l}{2}\qquad\theta\in[-\gamma,\theta_{c1}]. \tag{36}$$

Substituting the expressions for M, H, and G from (11) into $C_\tau(\theta,\mu)$ and $D_\tau(\theta,\dot\theta)$ specified in (15) gives

$$C_\tau(\theta,\mu)=\mu(e-\frac{2m_2}{m_1+m_2}h)+\frac{m_1}{m_{eq}}h\sqrt{1+\mu^2}\sin(\theta+\gamma)\cos(\theta)$$
$$D_\tau(\theta,\dot\theta)=-m_1r_{eq}\dot\theta^2h\sin\theta.$$

First consider $D_\tau(\theta,\dot\theta)$. Since $-\sin\gamma\leq\sin\theta<0$ and $\dot\theta^2\leq\dot\theta_{c1}^2$ in $\mathcal{R}_1^+$,

$$0<D_\tau(\theta,\dot\theta)\leq m_1r_{eq}\dot\theta_{c1}^2\sin\gamma.$$

According to Lemma 5.2, $f_n(t)\geq f_n^0$ for $t\in[0,t_A]$. Using the bounds on D_τ and f_n, the inequalities specified in (36) are satisfied when

$$|C_\tau(\theta,\mu)|+\frac{m_1r_{eq}\dot\theta_{c1}^2\sin\gamma}{f_n^0}\leq\frac{l}{2}\qquad\theta\in[-\gamma,\theta_{c1}]. \tag{37}$$

The derivative $C'_\tau(\theta,\mu)$ is strictly positive for $\theta\in[-\gamma,\theta_{c1}]$. Hence $C_\tau(\theta,\mu)$ is monotonically increasing and satisfies $C_\tau(-\gamma,\mu)\leq C_\tau(\theta,\mu)\leq C_\tau(\theta_{c1},\mu)$ in $[-\gamma,\theta_{c1}]$. It follows $|C_\tau(\theta,\mu)|\leq\max\{C_\tau(-\gamma,\mu),C_\tau(\theta_{c1},\mu)\}$. When this bound is substituted into (37), one obtains the lower bound on l. □

A rough estimate of the slider's minimal length for $r_1\neq0$ is as follows. Consider the line contact condition (35), $|C_\tau+D_\tau/f_n+r_1|\leq l/2$. When a dynamic jamming trajectory approaches the critical corner point p_c, the normal reaction force grows unbounded. Moreover, it can verified that D_τ is non-vanishing in $\mathcal{R}_1^+$. Hence the fraction D_τ/f_n becomes negligible relative to C_τ as the trajectory approaches p_c, and (35) becomes

$$l\geq 2\big(\max\{C_\tau(-\gamma,\mu),C_\tau(\theta_{c1},\mu)\}+r_1\big). \tag{38}$$

When the specific values of Table 4 are substituted into (38) with $\mu=0.47$, one obtains that $l>104.1$ mm, which is satisfied by the length $l=200$ mm listed in the table.

On the occurrence of a tipover motion: Consider the reduced dynamics of the IPOS mechanism in the $(\theta,\dot\theta)$ plane, eq. (19). According to Lemma 4.2, all solutions of (19) reach the curve $A(\theta,\dot\theta)=0$ in finite time $t=t_A$. However, any solution which reaches the curve $A(\theta,\dot\theta)=0$ *away* from the critical corner point p_c, must violate the line contact condition (35) at an *earlier time*, for the following reason. Let the normal reaction force distribution be lumped into a single normal force acting on the slider at a point $\boldsymbol{x}$. The signed distance of $\boldsymbol{x}$ from the slider's origin, x_τ, is given by $x_\tau=\tau/f_n$. Substituting $\tau=C_\tau f_n+D_\tau$ and $f_n=A/B$ gives $x_\tau(\theta,\dot\theta)=C_\tau(\theta,\mu)+B(\theta,\mu)D_\tau(\theta,\dot\theta)/A(\theta,\dot\theta)$. Since the trajectory reaches the curve $A(\theta,\dot\theta)=0$ away from p_c, $B(\theta,\mu)>0$ along this trajectory. Moreover, it can be verified that $D_\tau(\theta,\dot\theta)$ is non-vanishing in $\mathcal{R}_1^+$. It follows that $|x_\tau|\to\infty$ as $A(\theta(t),\dot\theta(t))\to0$. Hence there exists a time $t'_A<t_A$ at which (35) is violated and the line contact is broken. The slider undergoes a tipover motion at $t=t'_A$ followed by transition to single-contact sliding or contact separation.

6 Dynamic Simulation Results

This section describes simulations which demonstrate the feasibility of dynamic jamming in the IPOS mechanism. The simulations are based on the physical parameter values of Table 4. When these values are substituted into the mechanism's mass distribution parameter, κ, one obtains that $\mu_{min}=\sqrt{\kappa^2-1}=0.44$. Any friction coefficient above 0.44 is associated with the existence of solution inconsistency (Theorem 1). The same parameter values give $\mu_c=2\mu_{min}/\sqrt{3}=0.51$. Any μ above 0.51 is associated with the existence of dynamic jamming trajectories that reach the critical corner point p_c in finite time $t=t_A$ (Theorem 1). The simulations study the mechanism's behavior for μ lying in $[\mu_{min},\mu_c]$, and for μ larger than μ_c. They were implemented by using an event-driven ODE45 procedure in MATLAB, for the equation (19) as well as its time-scaled counterpart (23) which enables more accurate solution in the vicinity of p_c.

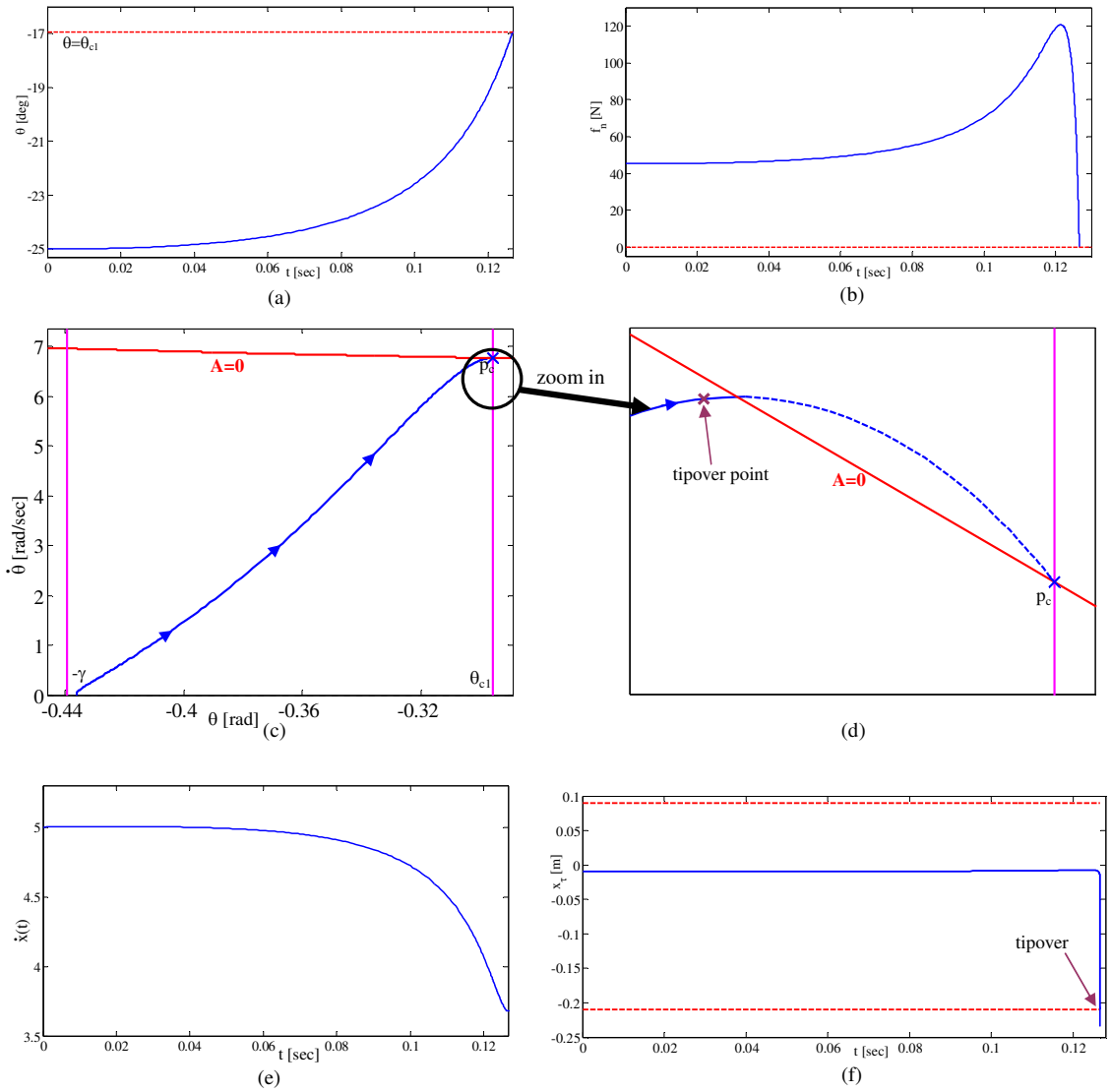

Fig. 7 A forward sliding motion of the IPOS mechanism corresponding to $\mu \in [\mu_{min}, \mu_c]$. (a) The hinge angle $\theta(t)$, (b) the normal force $f_n(t)$, (c)-(d) the $(\theta, \dot{\theta})$-plane trajectory, (e) the sliding velocity $\dot{x}(t)$, and (f) the torque arm $x_\tau(t)$.

First consider a friction coefficient $\mu = 0.47$, which lies in $[\mu_{min}, \mu_c]$. The critical angles bounding the solution inconsistency region (the solutions of $B(\theta, \mu) = 0$) are $\theta_{c1} = -16.94°$ and $\theta_{c2} = -8.23°$. The friction cone half-angle is $\gamma = 25.17°$, and the region $\mathcal{R}_1^+$ is bounded by $-25.17° \leq \theta \leq -16.94°$. Starting with initial conditions $\theta(0) = -25°$, $\dot{\theta}(0) = 0$, and $\dot{x}(0) = 5$ m/sec, the mechanism's full dynamics, eq. (10), was simulated under the sliding constraint $a_n = 0$. Figure 7(a) plots the hinge angle, $\theta(t)$, which seems to approach θ_{c1} within a finite time interval $[0, t_A]$, where $t_A = 0.126613$ sec. The normal contact force, $f_n(t)$, is plotted in Figure 7(b). It shows a bump in $f_n(t)$ followed by sharp decrease towards zero while the curve $A(\theta, \dot{\theta}) = 0$ is approached at $t = t_A$. Figure 7(c) plots the mechanism's phase-plane trajectory along with the curve $A(\theta, \dot{\theta}) = 0$ and the vertical line $\theta = \theta_{c1}$. A closeup view of the critical corner point vicinity is shown in Figure 7(d). It can be seen that the mechanism's trajectory crosses the curve $A(\theta, \dot{\theta}) = 0$ *before* reaching p_c. This behavior is in agreement with the predictions of Theorem 1. That is, when $\mu_{min} < \mu < \mu_c$ all trajectories that start in $\mathcal{R}_1^+$ cross the curve $A(\theta, \dot{\theta}) = 0$ before reaching p_c. Nevertheless, these plots represent the solution of the differential equation (19) that does not account for the additional inequality constraints on he tangential velocity $\dot{x} > 0$ and on the line contact torque τ in (13). Figure 7(e) plots the tangential sliding velocity, $\dot{x}(t)$, which remains positive during this time interval. Figure 7(f) plots the arm, $x_\tau(t)$, of the torque generated on the slider by the normal reaction force. The two horizontal lines in the figure represent the bounds that keep x_τ within the contact segment (and hence keep the line contact). Close look at the simulation results reveals that the line contact con-

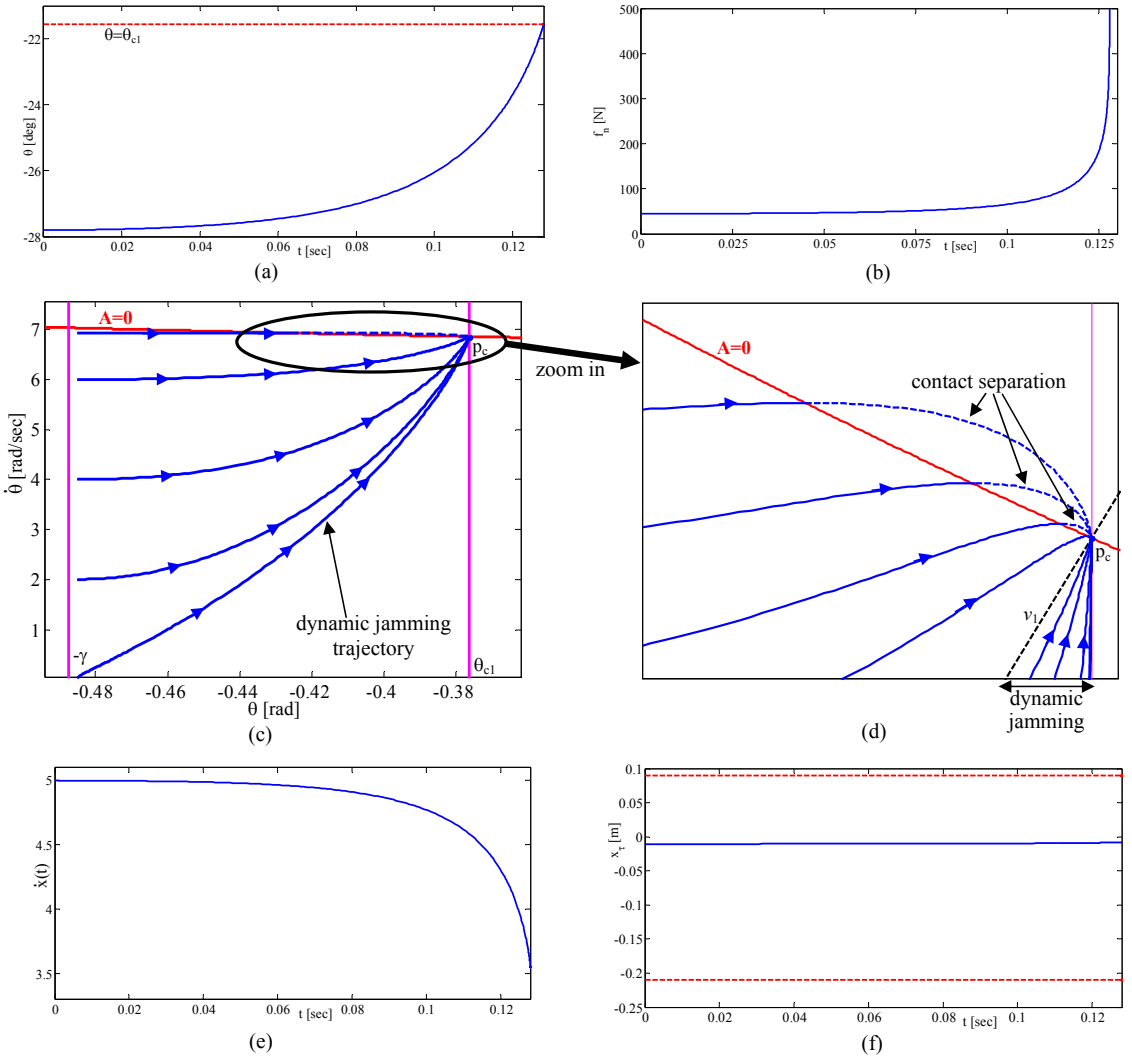

Fig. 8 Dynamic jamming trajectories of the IPOS mechanism for $\mu > \mu_c$. (a)-(b) The hinge angle $\theta(t)$ and the normal force $f_n(t)$ along a particular dynamic jamming trajectory. (c)-(d) Several $(\theta, \dot{\theta})$-plane trajectories. (e)-(f) The sliding velocity $\dot{x}(t)$ and the torque arm $x_\tau(t)$ along the dynamic jamming trajectory.

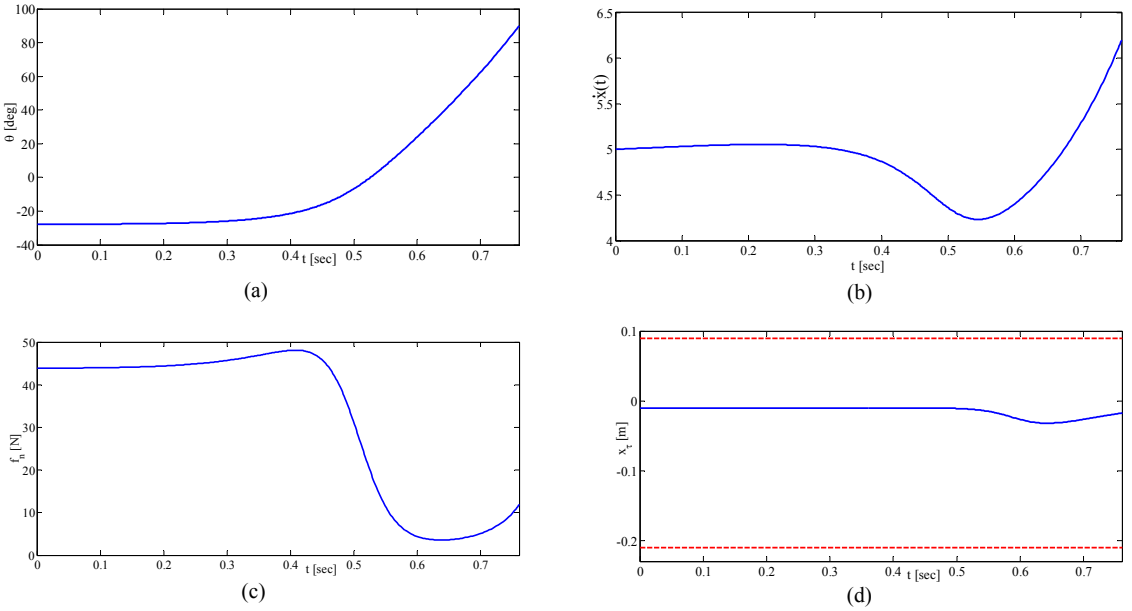

Fig. 9 Dynamic simulation of the IPOS mechanism with the rod having a uniform mass distribution.

dition (13) is violated at $t'_A = 0.126611 < t_A$. The slider then undergoes a tipover motion at $t = t'_A$ followed by transition to single-contact sliding or contact separation, *before* the contact separation curve $A=0$ is reached, in agreement with the observation in Section 5.2. The point at which tipover motion occurs is marked by '×' on the phase plane closeup view in 7(d). From this point and on, the solution of the system actually departs from the phase plane trajectory, since the governing equation (19) is no longer valid.

Next consider a friction coefficient $\mu = 0.53$, which is higher than $\mu_c = 0.51$. The two critical angles in this case are $\theta_{c1} = -21.56°$ and $\theta_{c2} = -6.36°$. The friction cone half-angle is $\gamma = 27.92°$, and the region $\mathcal{R}_1^+$ is bounded by $-27.92° \leq \theta \leq -21.56°$. Starting with $\theta(0) = -27.8°$, $\dot{\theta}(0) = 0$, and $\dot{x}(0) = 5$ m/sec, the mechanism's trajectory was computed with eq. (10) under the sliding constraint $a_n = 0$. Figures 8(a) plots the hinge angle, $\theta(t)$, which again approaches θ_{c1} within a finite time interval. Figure 8(b) plots the normal contact force, $f_n(t)$, showing that it grows unbounded in finite time. This is precisely the dynamic jamming event. Figure 8(c) plots several phase plane trajectories associated with different initial conditions in $\mathcal{R}_1^+$. Figure 8(d) shows a closeup view of the vicinity of the critical point. It reveals that some trajectories converge to the critical corner point p_c, leading to dynamic jamming, while others cross the curve $A(\theta, \dot{\theta}) = 0$, leading to contact separation. In the latter case, crossing the separation curve is actually unphysical since tipover motion will occur first, as explained in the previous simulation example. Note that trajectories that start below the eigenvector $\boldsymbol{v}_1$ of the linearized dynamics reach the point p_c, as predicted in Section 4. Figures 8(e)-(f) return to the dynamic jamming trajectory associated with the initial conditions specified above. The figures plot the slider's tangential velocity, $\dot{x}(t)$, and the arm of the net torque, $x_\tau(t)$. The figures corroborate that the mechanism keeps its forward sliding motion as well as its line contact during the time interval leading to dynamic jamming.

To emphasize the influence of the rod's mass distribution on the occurrence of dynamic jamming, consider the mechanism's trajectory when the rod has a *uniform* mass distribution. The rod's radius of gyration in this case is $\rho_2 = r_2/\sqrt{3}$, where r_2 is the rod's half length. All other parameters were left unchanged, and the coefficient of friction is $\mu = 0.53$ as before. The minimal friction coefficient associated with solution inconsistency is now $\mu_{min} = 1.43$. Since $\mu < \mu_{min}$, dynamic jamming is now infeasible. Figure 9 shows the time plots of $\theta(t)$, $f_n(t)$, $\dot{x}(t)$, and $x_\tau(t)$. The simulations were stopped after θ has monotonically increased to $+90°$, where the rod physically hits the inclined plane. It can be seen that a consistent sliding motion was maintained at all times, with f_n remaining strictly positive and finite at all times. The occurrence of dynamic jamming thus depends on the rod having a *non-uniform* mass distribution. When $\rho_2 \ll r_2$ in the IPOS mechanism, μ_{min} and μ_c attain practical values such as 0.44 and 0.51.

7 Concluding Discussion

This paper investigated the sliding dynamics of the IPOS mechanism, which mimics Painlevé's sliding rod but requires a significantly lower contact friction to achieve dynamic jamming. The mechanism's dynamics under line distribution of frictional contact forces was formulated, and the occurrence of Painlevé's paradox was analyzed. The minimal friction coefficient, μ_{min}, for which Painlevé's paradox is possible was derived. Then the critical friction coefficient, μ_c, above which solutions may approach the region of inconsistency (and hence dynamic jamming) was identified. When $\mu < \mu_c$ the contact force always tends to zero, while contact separation is preceded by tipover motion. When $\mu > \mu_c$ there exists a region of initial conditions from which the contact force grows unbounded in finite time, resulting in dynamic jamming . Focusing on the IPOS mechanism, we derived a lower bound on the initial sliding velocity guaranteeing that the mechanism will retain its forward sliding motion, as well as a lower bound on the slider's length guaranteeing line contact during the time interval leading to dynamic jamming. Dynamic simulation results corroborate the analysis and demonstrate the feasibility of achieving dynamic jamming with the IPOS mechanism under practical friction conditions.

Preliminary motion experiments with the IPOS mechanism prototype shown in Figure 4 were reported in [22]. Unfortunately, it turns out that the current prototype operates with friction coefficient in the range $\mu_{min} < \mu < \mu_c$. As discussed earlier in the paper, when μ lies in this range the mechanism's slider undergoes a tipover motion followed by contact separation, but dynamic jamming is infeasible. The IPOS prototype is currently undergoing mechanical design improvements so that μ_c (which depends on the mechanism's overall mass distribution parameter κ) would satisfy the condition $\mu > \mu_c$, and thus allow dynamic jamming. Based on the analysis and simulations conducted in this paper, the improved prototype will be able to exhibit dynamic jamming trajectories, and to demonstrate this phenomenon

experimentally for the first time. If such experiments will prove successful, they will show that Painlevé's paradox is a real-world physical phenomenon, and that the rigid body model and Coulomb friction law provide a faithful description of the mechanism's dynamics.

Future extensions include investigation of other aspects of Painlevé's paradox. For instance, one needs to experimentally investigate the velocity and contact force changes during tangential impact, and compare the actual measurements to various theoretical models of frictional impact available in the literature (e.g. [3,24,36,37]). Another extension is studying the occurrence of Painlevé's paradox and dynamic jamming under transitions between line-contact sliding, point-contact sliding, and tangential sticking.

Finally, a long-term future goal is generalization of the theory to multiple contacts and to three dimensions. This extension will provide important tools for assessing the safety and stability of robotic tasks with dynamic contact transitions such as legged robot locomotion over variable geometry terrains, as well as robotic manipulation and grasping systems.

A Proof Details

This appendix contains proofs of auxiliary lemmas from Sections 4 and 5. The first lemma derives the reduced dynamics of the IPOS mechanism in the $(\theta,\dot\theta)$ plane.

Lemma 4.1 *The dynamics of the IPOS hinge angle θ is given by*

$$\ddot\theta = C(\theta,\mu)\frac{A(\theta,\dot\theta)}{B(\theta,\mu)}, \tag{39}$$

where

$$A(\theta,\dot\theta) = g\cos\alpha - r_{eq}\dot\theta^2\cos\theta$$

$$B(\theta,\mu) = \frac{1}{m_{eq}}\Big(\tfrac{1}{2}(\kappa+1) - \cos^2\theta + \mu\sin\theta\cos\theta\Big) \tag{40}$$

$$C(\theta,\mu) = \frac{\sqrt{1+\mu^2}}{m_{eq}r_{eq}}\sin(\theta+\gamma).$$

Proof: To derive the dynamic equation of θ, consider the solution for $\ddot q$ from (10),

$$\ddot q = -M^{-1}(q)\big(H(q,\dot q)+G(q)\big)+f_nM^{-1}(q)\big(\boldsymbol{w}_n(q)-\sigma\mu\boldsymbol{w}_t(q)\big) +\tau M^{-1}(q)\boldsymbol{w}_\psi.$$

The hinge acceleration, $\ddot\theta$, is the third coordinate of $\ddot q$. Hence $\ddot\theta = \boldsymbol{w}_\theta\cdot\ddot q$ where $\boldsymbol{w}_\theta = (0,0,1,0)$. The governing equation during consistent sliding takes the form $0=-A+Bf_n$. Hence $f_n = A/B$. Substituting for f_n and for τ according to (7), the dynamics of θ is given by

$$\ddot\theta = \boldsymbol{w}_\theta\cdot\ddot q = C(q,\mu)\frac{A(q,\dot q)}{B(q,\mu)} + D(q,\dot q).$$

where $C(q,\mu)=\boldsymbol{w}_\theta^TM^{-1}(q)W(q)\big(\boldsymbol{w}_n(q)-\sigma\mu\boldsymbol{w}_t(q)\big)$ and $D(q,\dot q)=-\boldsymbol{w}_\theta^TM^{-1}(q)W(q)\big(H(q,\dot q)+G(q)\big)$. Substituting for M, H, and G according to (11) gives

$$C(\theta,\mu) = \frac{\sqrt{1+\mu^2}r_2}{m_1(r_2^2+\rho_2^2)+m_2\rho_2^2}\sin(\theta+\gamma),$$

while $D=0$. Finally, $A(\theta,\dot\theta)$ and $B(\theta,\mu)$ are obtained by substituting $\sigma=1$ in (12),

$$A(\theta,\dot\theta) = g\cos\alpha - r_{eq}\dot\theta^2\cos\theta$$

$$B(\theta,\mu)=\frac{1}{m_{eq}}\left(\big(1+\frac{m_1}{m_2}\big)\big(1+\frac{\rho_2^2}{r_2^2}\big)-\cos^2\theta+\mu\sin\theta\cos\theta\right).$$

□

The second lemma provides a lower bound on the normal reaction force, f_n, during dynamic jamming trajectories of the IPOS mechanism.

Lemma 5.2 *Let the IPOS mechanism start sliding with $(\theta(0),\dot\theta(0))\in\mathcal{R}_1^+$ and reach the critical corner point $p_c=(\theta_{c1},\dot\theta_{c1})$ at $t=t_A$. The normal reaction force along this trajectory satisfies the lower bound*

$$f_n(t) \geq \frac{1}{\mu}m_{eq}g\cos\alpha\,|\tan(\theta_{c1})| \quad \text{for } t\in[0,t_A],$$

where $\mu>\mu_c$ is the friction coefficient and α is the inclined plane slope angle.

Proof: Since $0=-A+Bf_n$ during sliding, $f_n(\theta,\dot\theta)=A(\theta,\dot\theta)/B(\theta,\mu)$. Consider the set $\mathcal{S}=\{(\theta,\dot\theta)\in\mathcal{R}_1^+ : f_n(\theta,\dot\theta)\geq f_n^0\}=\{(\theta,\dot\theta)\in\mathcal{R}_1^+ : A(\theta,\dot\theta)/B(\theta,\mu)\geq f_n^0\}$. Using the fact that $B\geq 0$ in $\mathcal{R}_1^+$ and substituting $A(\theta,\dot\theta)=g\cos\alpha - r_{eq}\dot\theta^2\cos\theta$,

$$\mathcal{S}=\left\{\begin{pmatrix}\theta\\ \dot\theta\end{pmatrix}\in\mathcal{R}_1^+ : \dot\theta^2\leq\frac{1}{r_{eq}\cos\theta}\big(g\cos\alpha - f_n^0B(\theta,\mu)\big)\right\}.$$

Consider a dynamic jamming trajectory, $(\theta(t),\dot\theta(t))$, which starts at $(\theta(0),\dot\theta(0))\in\mathcal{R}_1^+$ and reaches the point $p_c=(\theta_{c1},\dot\theta_{c1})$ at $t=t_A$. Since $\dot\theta(t)$ is monotonically increasing with t and $\dot\theta(t_A)=\dot\theta_{c1}$, $\dot\theta(t)\leq\dot\theta_{c1}$ for $t\in[0,t_A]$. When the boundary curve of $\mathcal{S}$ lies *above* the line $\dot\theta=\dot\theta_{c1}$ in the $(\theta,\dot\theta)$ plane, the trajectory $(\theta(t),\dot\theta(t))$ lies in $\mathcal{S}$ for $t\in[0,t_A]$ (and hence $f_n(t)\geq f_n^0$ for $t\in[0,t_A]$). The boundary curve of $\mathcal{S}$ lies above $\dot\theta=\dot\theta_{c1}$ when is satisfies the inequality

$$\frac{1}{r_{eq}\cos\theta}\big(g\cos\alpha - f_n^0B(\theta,\mu)\big)\geq\dot\theta_{c1}^2.$$

Since $\cos\theta>0$ in $\mathcal{R}_1^+$, the inequality can be written as

$$g\cos\alpha - f_n^0B(\theta,\mu)\geq r_{eq}\dot\theta_{c1}^2\cos\theta.$$

Define $F(\theta)=g\cos\alpha - f_n^0B(\theta,\mu) - r_{eq}\dot\theta_{c1}^2\cos\theta$. Since $F(\theta_{c1})=0$, a sufficient condition for $F(\theta)\geq 0$ in the interval $[-\gamma,\theta_{c1}]$ is that the derivative, $F'(\theta)$, be non-positive:

$$F'(\theta) = -f_n^0B'(\theta,\mu) + r_{eq}\dot\theta_{c1}^2\sin\theta\leq 0.$$

Using expression (16) for B, $B'(\theta,\mu)=\sqrt{1+\mu^2}\sin(2\theta+\gamma)/m_{eq}$. The term $B'(\theta,\mu)$ is thus monotonically increasing and negative for $\theta\in[-\gamma,\theta_{c1}]$. Hence $|B'(\theta,\mu)|\leq|B'(-\gamma,\mu)|$. Substituting $|B'(-\gamma,\mu)|=\tan\gamma/m_{eq}$ and using the fact that

$|\sin\theta| > |\sin(\theta_{c1})|$ in $[-\gamma, \theta_{c1}]$, the condition $F'(\theta) \leq 0$ (and hence $F(\theta) \geq 0$) holds when f_n^0 satisfies the inequality

$$f_n^0 \leq r_{eq} m_{eq} \dot{\theta}_{c1}^2 \frac{|\sin(\theta_{c1})|}{\tan\gamma}. \tag{41}$$

The set $\mathcal{S} = \{(\theta, \dot{\theta}) \in \mathcal{R}_1^+ : f_n(\theta, \dot{\theta}) \geq f_n^0\}$ such that f_n^0 satisfies (41) contains the portion of $\mathcal{R}_1^+$ lying below the $\dot{\theta} = \dot{\theta}_{c1}$ line. Hence $f_n(t) \geq r_{eq} m_{eq} \dot{\theta}_{c1}^2 |\sin(\theta_{c1})| / \tan\gamma$ along all dynamic jamming trajectories. Substituting $\dot{\theta}_{c1}^2 = g\cos\alpha / r_{eq}\cos(\theta_{c1})$ and $\mu = \tan\gamma$ gives the upper bound specified in the lemma. □

References

1. M. Anitescu and F. A. Potra. Formulating dynamic multi-rigid-body contact problems with friction as solvable linear complementarity problems. *Nonlinear Dynamics*, 14:231–247, 1997.
2. B. Brogliato. *Nonsmooth Mechanics*. Springer-Verlag, 1999.
3. A. Chatterjee and A. Ruina. A new algebraic rigid body collision law based on impulse space considerations. *Journal of Applied Mechanics*, 65(4):939–951, 1998.
4. S. H. Collins, M. Wisse, and A. Ruina. A 3-D passive dynamic walking robot with two legs and knees. *International Journal of Robotics Research*, 20:607–615, 2001.
5. M. diBernardo, C. J. Budd, A. R. Champneys, and P. Kowalczyk. *Piecewise-smooth Dynamical Systems: Theory and Applications*. Springer, 2007.
6. P. E. Dupont. The effect of Coulomb friction on the existence and uniqueness of the forward dynamics problem. In *IEEE Int. Conf. on Robotics and Automation*, pages 1442–1447, 1992.
7. P. E. Dupont and S. P. Yamajako. Jamming and wedging in constrained rigid-body dynamics. In *Proc. IEEE Int. Conf. on Robotics and Automation*, pages 2349–2354, 1994.
8. M. A. Erdmann. An exploration of nonprehensile two-palm manipulation. *The Int. J. of Robotics Research*, 17(5):485–503, 1998.
9. A. Filippov. *Differential equations with discontinuous right-hand sides*. Kluwer Academic Publishers, 1988.
10. F. Génot and B. Brogliato. New results on Painlevé paradoxes. *Eu. J. Mechanics A/Solids*, 18(4):653–677, 1999.
11. R. Goebel, R. G. Sanfelice, and A. R. Teel. Hybrid dynamical systems. *IEEE Control Systems Magazine*, 29(2):28–93, 2009.
12. B. Hall and A. Champneys. Why does chalk squeak? Technical report, Dept. of Eng. Math., University of Bristol, 2009, in `www.enm.bris.ac.uk/teaching/projects/2008_09/bh5217/download/Chalk_Report.pdf`.
13. Y. Hurmuzlu, F. Génot, and B. Brogliato. Modeling, stability and control of biped robots—a general framework. *Automatica*, 40(10):1647–1664, 2004.
14. P. R. Kraus, V. Kumar, and P. Dupont. Analysis of frictional contact models for dynamic simulation. In *IEEE Int. Conf. on Robotics and Automation*, pages 2822–2827, 1998.
15. R. I. Leine, B. Brogliato, and H. Nijmeijer. Periodic motion and bifurcations induced by the Painlevé paradox. *European Journal of Mechanics– A/Solids*, 21:869–896, 2002.
16. R. I. Leine and H. Nijmeijer. *Dynamics and bifurcations of non-smooth mechanical systems*. Springer, 2004.
17. C. Liu, Z. Zhao, and B. Chen. The bouncing motion appearing in a robotic system with unilateral constraint. *Nonlinear Dynamics*, 49:217–232, 2007.
18. S. Lohmeier, T. Buschmann, H. Ulbrich, and F. Pfeiffer. Humanoid robot LOLA - research platform for high-speed walking. In H. Ulbrich and L. Ginzinger, editors, *Motion and Vibration Control: Selected Papers from MOVIC 2008*, pages 221–230. Springer, 2009.
19. P. Lotstedt. Coulomb friction in two-dimensional rigid body systems. *Zeitschrift fur Angewandte Mathematik und Mechanik*, 61:605–615, 1981.
20. Kevin M. Lynch and M. T. Mason. Dynamic nonprehensile manipulation: Controllability, planning, and experiments. *International Journal of Robotics Research*, 18(1):64–92, 1999.
21. M. T. Mason and Y. Wang. On the inconsistency of rigid-body frictional planar mechanics. In *IEEE Int. Conf. on Robotics and Automation*, pages 524–528, 1988.
22. D. Meltz, Y. Or, and E. Rimon. Experimental verification and graphical characterization of dynamic jamming in frictional rigid-body mechanics. In *IEEE Int. Conf. on Robotics and Automation*, pages 580–585, 2007.
23. J. J. Moreau. Unilateral contact and dry friction in finite freedom dynamics. In *Nonsmooth Mechanics and Applications*, volume 302 of *CISM Courses and lectures*, pages 1–82. Springer-Verlag, 1988.
24. A. Nordmark, H. Dankowicz, and A. Champneys. Discontinuity-induced bifurcations in systems with impacts and friction: Discontinuities in the impact law. *Int. J. Non-Linear Mechanics*, 44:1011–1023, 2009.
25. A. Nordmark, H. Dankowicz, and A. Champneys. Friction-induced reverse chatter in rigid-body mechanisms with impacts. *IMA Journal of Applied Mathematics*, 76(1):85–119, 2011.
26. Y. Or and A. D. Ames. Stability of Zeno equlibria in Lagrangian hybrid systems. In *Proc. IEEE Conf. on Decision and Control*, pages 2770–2775, 2008.
27. P. Painlevé. Sur les lois du frottement de glissement. *C. R. Acad. Sci. Paris*, (121):112–115, 1895.
28. J.-S. Pang. Frictional contact models with local compliance: Semismooth formulation. *Zeitschrift fur Angewandte Mathematik und Mechanik*, 88(6):454–471, 2008.
29. J.S. Pang and J.C. Trinkle. Complementarity formulations and existence of solutions of dynamic multi-rigid-body contact problems with Coulomb friction. *Mathematical Programming*, 74:199–226, 1996.
30. F. Pfeiffer and C. Glocker. *Multibody Dynamics with Unilateral Contacts*. John Wiley & Sons, New York, 1996.
31. R. Segev and A. Ailon. A geometrical setting for the newtonian mechanics of robots. *J. of the Franklin Institute*, 322(3):173–183, Sept 1986.
32. P. Song, J.-S. Pang, and V. Kumar. A semi-implicit time-stepping model for frictional compliant contact problems. *International Journal for Numerical Methods in Engineering*, 60(13):2231–2261, 2004.
33. D. E. Stewart and J. C. Trinkle. An implicit time-stepping scheme for rigid body dynamics with inelastic collisions and Coulomb friction. *Int. J. of Numerical Methods in Engineering*, 39:2673–2691, 1996.
34. D.E. Stewart. Convergence of a time-stepping scheme for rigid body dynamics and resolution of painlevé's problem. *Archive for Rational Mechanics and Analysis*, 145(3):215–260, 1998.
35. D.E. Stewart. Rigid-body dynamics with friction and impact. *SIAM Review*, 41(1):3–39, 2000.
36. W. J. Stronge. *Impact Mechanics*. Cambridge University Press, Cambridge, UK, 1979.
37. Y. Wang and M. T. Mason. Two-dimensional rigid body collisions with friction. *J. of Applied Mechanics*, 10:292–352, 1993.
38. E. R. Westervelt, J. W. Grizzle, C. Chevallereau, J. H. Choi, and B. Morris. *Feedback Control of Dynamic Bipedal Robot Locomotion*. CRC Press, 2007.

39. E. V. Wilms and H. Cohen. The occurence of Painlevés paradox in the motion of a rotating shaft. *Journal of Applied Mechanics*, 64:1008–1010, 1997.
40. J. Zhang, K. H. Johansson, J. Lygeros, and S. Sastry. Zeno hybrid systems. *Int. J. Robust and Nonlinear Control*, 1(2):435–451, 2001.
41. Z. Zhao, C. Liu, W. Ma, and B. Chen. Experimental investigation of the Painlevé paradox in a robotic system. *Journal of Applied Mechanics*, 75:041006, 2007.